Evaluation of Bioink Printability for Bioprinting Applications

Zhengyi Zhang¹, Yifei Jin², Jun Yin³, Changxue Xu⁴, Ruitong Xiong², Kyle Christensen², Bradley R. Ringeisen⁵, Douglas B. Chrisey⁶, and Yong Huang^{2,7,8,*}

¹School of Naval Architecture and Ocean Engineering, Huazhong University of Science and Technology, Wuhan 430074, PR China

²Department of Mechanical and Aerospace Engineering, University of Florida, Gainesville, FL 32611, USA

³College of Mechanical Engineering, Zhejiang University, Hangzhou 310028, China
⁴Department of Industrial, Manufacturing, and Systems Engineering, Texas Tech University,
Lubbock, TX 79409, USA

⁵Defense Advanced Research Projects Agency, Arlington, VA 22203, USA

⁶Department of Physics and Engineering Physics, Tulane University, New Orleans, LA 70118,

USA

⁷Department of Materials Science and Engineering, University of Florida, Gainesville, FL 32611, USA

⁸Department of Biomedical Engineering, University of Florida, Gainesville, FL 32611, USA *Corresponding author, Department of Mechanical and Aerospace Engineering, University of Florida, Gainesville, FL 32611, USA, Phone: 001-352-392-5520, Fax: 001- 352-392-7303, Email: yongh@ufl.edu

Abstract

Three-dimensional (3D) bioprinting, as a freeform biomedical manufacturing approach, has been increasingly adopted for the fabrication of constructs analogous to living tissues. Generally, materials printed during 3D bioprinting are referred as bioinks, which may include living cells, extracellular matrix materials, cell media, and/or other additives. For 3D bioprinting to be an enabling tissue engineering approach, the bioink printability is a critical requirement as tissue constructs must be able to be printed and reproduce the complex micro-architecture of native tissues in vitro in sufficient resolution. The bioink printability is generally characterized in terms of the controllably formation of well-defined droplets/jets/filaments and/or the morphology and shape fidelity of deposited building blocks. This review presents a comprehensive overview of the studies of bioink printability during representative 3D bioprinting processes, including inkjet printing, laser printing, and micro-extrusion, with a focus on the understanding of the underlying physics during the formation of bioink-based features. A detailed discussion is conducted based on the typical time scales and dimensionless quantities for printability evaluation during bioprinting. For inkjet printing, the Z (the inverse of the Ohnesorge number), Weber, and capillary numbers have been employed for the construction of phase diagrams during the printing of Newtonian fluids, while the Weissenberg and Deborah numbers have been utilized during the printing of non-Newtonian bioinks. During laser printing of Newtonian solutions, the jettability can be characterized using the inverse of the Ohnesorge number, while Ohnesorge, elasto-capillary, and Weber numbers have been utilized to construct phase diagrams for typical non-Newtonian bioinks. For micro-extrusion, seven filament types have been identified including three types of well-defined filaments and four types of irregular filaments. During micro-extrusion, the Oldroyd number has been used to characterize the dimensions of the yielded

areas of Herschel-Bulkley fluids. Non-ideal jetting behaviors are common during the droplet-based inkjet and laser printing processes due to the local nonuniformity and nonhomogeneity of cell-laden bioinks.

1. Introduction

The need for living tissues and organs for various biomedical applications has spurred the development of tissue engineering, seeking to create functional tissues and organs on demand.¹⁻⁴ The traditional tissue engineering approaches can be classified into two groups: scaffold-directed^{5,6} and scaffold-free.^{7,8} The classic scaffold-directed approach employs three-dimensional (3D) porous solid biodegradable scaffolds^{6,9,10} as synthetic extracellular matrix (ECM) to seed cells on their surface to form 3D cellular architectures, and the ECM is also used to present stimuli which direct the growth and formation of desired tissues.¹¹ On the other hand, the scaffold-free approach¹²⁻¹⁵ relies on biological self-assembly and self-organization of cells and especially microtissues to generate functional tissues without the need for a scaffold. In such an approach, cell clusters,¹² cell aggregates,¹⁴ or 2D cell sheets¹³ are formed and then assembled accordingly to create 3D cellular constructs without the help of a scaffold.

Although the classic scaffold-directed approach has been used to fabricate 2D/3D constructs, ¹⁶ it still faces some limitations and challenges: ¹⁶⁻¹⁸ 1) effective vascularization of thick tissue constructs, and 2) heterogeneously placing multiple cell types inside a scaffold. The scaffold-free approach also has some limitations, despite having a number of potential advantages over the scaffold-directed approach. Because of its scaffold-free nature, it is hard to fabricate complex organ-like structures with overhangs and to provide sufficient mechanical strength while ECM is

being generated by printed cells; furthermore, the fabrication of large cellular constructs using the scaffold-free approach is limited by the transport of oxygen, nutrients, and waste products until a vascular system develops.⁸ As an alternative solution, 3D bioprinting has been developed as a promising tissue engineering approach, which is enabled by recent advances in additive manufacturing (AM) technology, cellular biology, and materials science.⁴

Generally, materials for 3D bioprinting are referred as bioinks which may include living cells (either suspended or as cell aggregates), extracellular matrix materials such as applicable hydrogels, cell media, and/or other additives. Sometimes, the term of cell-laden bioinks is specifically adopted for cell and organ printing applications. During printing, bioinks are precisely deposited layer by layer by a bioprinter for the freeform fabrication of various 3D acellular or cellular constructs, which can be represented using computer-aided design (CAD) models of tissues/organs to be replaced. ¹⁹ Technically speaking, bioprinting can be further classified into direct and indirect bioprinting; direct bioprinting utilizes build materials containing living cells, while build materials during indirect bioprinting are acellular. ⁴

The basic philosophy of 3D bioprinting is to use AM methods to accurately position bioinks instead of traditional plastic and metal inks for fabrication applications. The overarching vision for 3D bioprinting-based organ printing is depicted in Figure 1, which includes three key steps: (1) imaging, (2) layer-by-layer bioprinting, and (3) tissue fusion and maturation. First, a comprehensive understanding of the functional tissues/organs is acquired in terms of CAD models with the help of noninvasive medical imaging technologies, such as magnetic resonance imaging (MRI, including micro MRI), computed tomography (CT, including micro CT), which

provide digital maps to describe the composition and organization of tissue/organ components. Then, slicer software is used to discretize the 3D CAD models into a series of 2D horizontal slices to guide layer-by-layer bioprinting, during which 3D constructs are obtained, reproducing the complex, heterogeneous architecture of tissues/organs of interest. Finally, functional printed tissues/organs are harvested after incubating the printed constructs in an appropriate environment, during which tissue fusion and maturation occur.

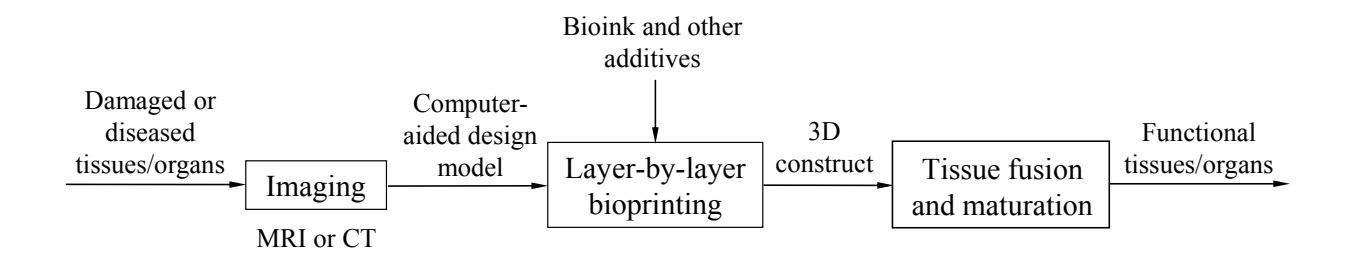


Figure 1. Key steps of 3D bioprinting-based organ biofabrication.

A feasible bioprinting approach should be able to work in an aqueous or aqueous-gel environment at temperatures ranging from room temperature to 38°C.⁸ While there is a wide range of AM techniques,²⁰ only a few can be employed for 3D direct bioprinting of cellular constructs by dispensing cell-laden bioinks, which requires the deposition process to be cytocompatible. Of them, inkjet printing, laser printing (laser-induced forward transfer or modified laser-induced forward transfer), and micro-extrusion (or extrusion as shown in Figure 2) are the three most commonly explored approaches for direct bioprinting as reported in the literature. The basic building blocks are bioink droplets during inkjet- and laser printing and bioink filaments during micro-extrusion. Therefore, these three bioprinting technologies can be

further classified into two groups: (1) droplet-based printing, which includes inkjet printing²¹ and laser printing,²² and (2) filament-based printing²³ as shown in Figure 2.

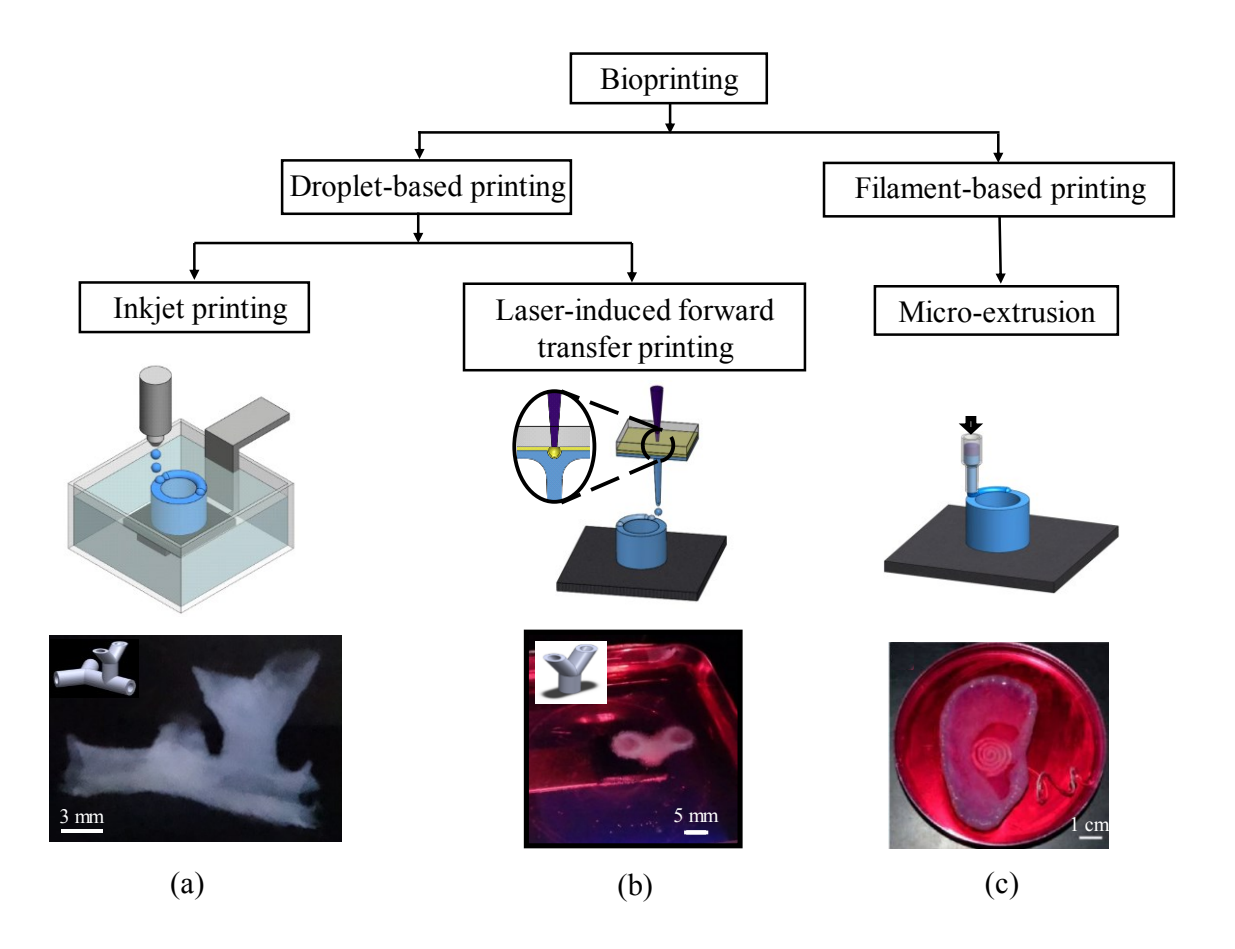


Figure 2. Three main 3D bioprinting techniques: (a) inkjet printing, (b) laser printing, and (c) micro-extrusion and representative products for each bioprinting technique: (a) an inkjet-printed fibroblast structure with both horizontal and vertical bifurcations, ²¹ (b) a laser-printed *Y*-shaped fibroblast tube, ²² (c) a micro-extruded bionic ear. ²³ Figures and captions are reproduced with permission from (1) Biotechnology and Bioengineering **112**, 1047 (2015). Copyright 2014 Wiley Periodicals, Inc., (2) Biofabrication **7**, 045011 (2015). Copyright 2015 IOP Publishing Ltd., and (3) Nano Letter **13**, 2634 (2013). Copyright 2013 American Chemical Society.

As a freeform fabrication approach, 3D bioprinting is technologically more advanced and potentially superior to traditional tissue engineering approaches in the following aspects: ¹⁸ 1) facilitating precise 3D positioning of different cells and direct control of cells' microenvironment, 2) enabling the fabrication of cellular constructs with high cell density, 3) generating porous living constructs with predetermined heterogeneity on demand and solving the mass transport problem in thick tissue constructs, and 4) offering a pathway to the reproducible, scalable, and mass production of tissues/organs. In the field of tissue engineering and regenerative medicine, bioprinting has already been employed to fabricate various living constructs, such as vascular-like living cellular constructs, ^{21,22,24} custom-shaped orthopedic prostheses and implants, ²⁵ and bionic ears, ²³ to name a few. Figure 2 gives some representative bio-printed products. In addition, bioprinting technology has a broad utility in a variety of application areas ⁴ such as precision medicine, ²⁶ medical devices, ²⁷ reactionware for chemical synthesis and analysis, ²⁸ drug screening and high throughput assays. ²⁹⁻³¹ and cancer research. ^{32,33}

The objective of this study is to review the characterization of bioink printability during representative 3D bioprinting processes, namely, droplet-based printing (in terms of inkjet printing and laser printing) and filament-based printing (in terms for micro-extrusion printing). Herein the bioink printability is characterized in terms of the controllable formation of well-defined droplets/jets/filaments and/or the morphology and shape fidelity of deposited building blocks. For 3D bioprinting to be an enabling tissue engineering approach, the bioink printability is a critical requirement as tissue constructs must be able to be printed and reproduce the complex micro-architecture of native tissues *in vitro* in sufficient resolution. In the past decade, while many bioink research efforts have been made to develop new bioink materials for better

biocompatibility and biofunctionality, the bioink printability is largely ignored and still needs to be carefully examined to enable robotic bioprinting. In this study, the printability during inkjet bioprinting is characterized based on its ability to generate well-defined single droplets in air. The printability of bioink during laser printing is defined as the ability to generate well-defined jets during the jet and droplet formation process as well as well-defined printed droplets on a receiving substrate during the jet and droplet deposition process. In extrusion-based bioprinting, the printability is defined as the capability of bioinks to form continuous filaments with a controllable diameter and well-defined morphology, which is considered the extrudability, and further form well-defined 3D structures, which is considered the formability. Generally, once a well-defined droplet or filament can be formed, it is feasible to produce 3D structures/constructs with good fidelity and integrity.

2. Importance of Bioink Printability for Bioprinting Implementation

Bioinks are fluidic biomaterials and/or biological materials loaded with living cells, and are the 'raw materials' for bioprinting. They should be compatible with applicable bioprinting technologies to fabricate functional living constructs with suitable biological and mechanical properties. As illustrated in Figure 3(a), important properties of ideal bioinks may include: (1) printability: bioink should be flowable or deformable and be able to be deposited precisely with a good spatial, temporal, and volumetric control; (2) biocompatibility: it should be able to provide a non-cytotoxic ECM environment to support the adhesion, signaling, proliferation, and/or differentiation of living cells while maintaining satisfactory post-printing cell viability. Furthermore, it should not cause immune responses in the host; (3) biomimicry: engineering of desired structural, functional and dynamic material properties should be based on knowledge of

tissue-specific endogenous material compositions;³⁴ (4) mechanical integrity and stability: the printed bioink material should retain its shape as printed, and the chemical and/or physical gelation mechanisms of bioinks during and after printing must be biocompatible with living cells; and (5) biodegradability: its degradation rate should match the ability of cells to produce their own ECM.³⁵ Compromised decision is often needed to design bioinks while it is hard to develop an ideal bioink that possesses all the aforementioned properties. In particular, the biofabrication window is a typical example to show the interplay among different bioink material properties (Figure 3(b)). For example, the *yz* panel of Figure 3(b) describes the compromises that have traditionally been made to design bioinks that have suboptimal, yet passable, print fidelity while maintaining cell viability.³⁶

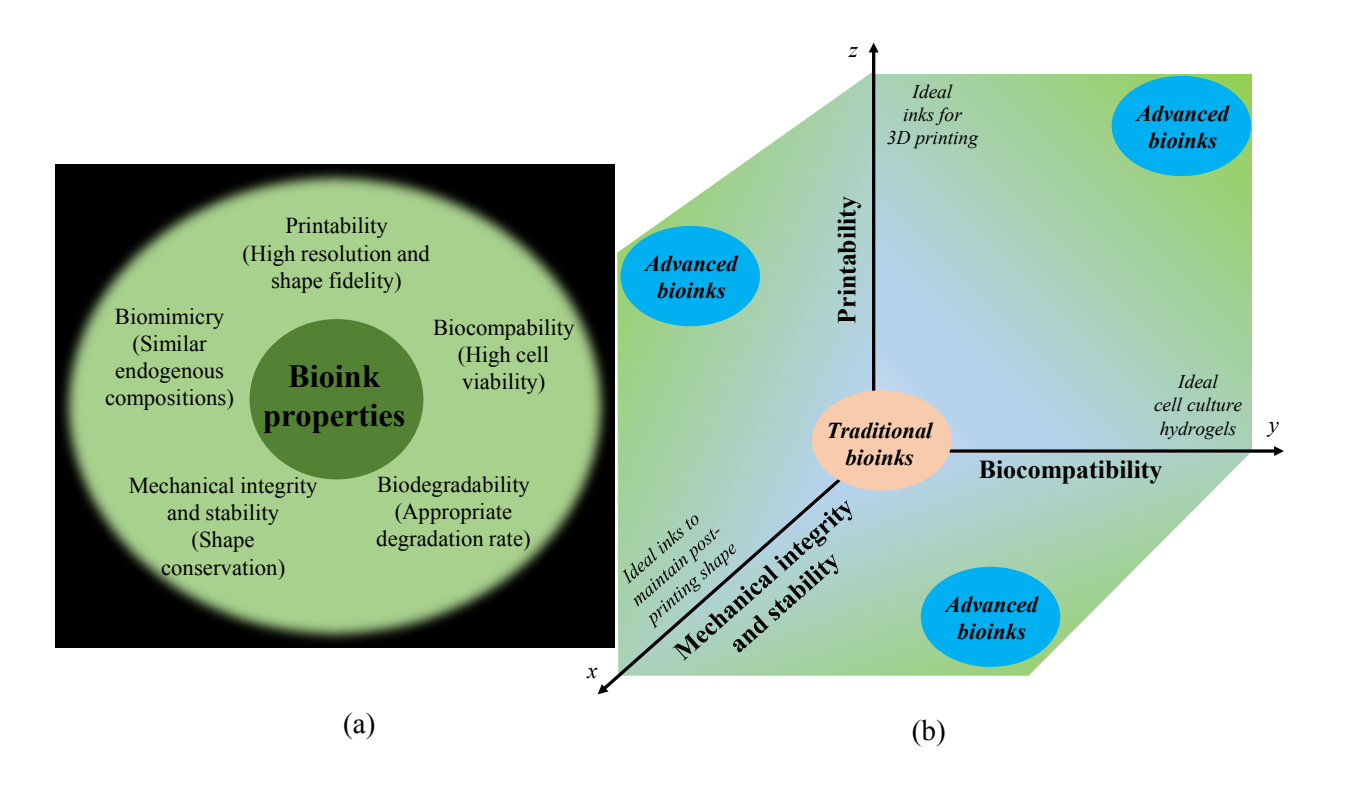


Figure 3. (a) Material properties for an ideal bioink and (b) biofabrication window for rational design of bioinks requiring compromise among different requirements.

Typical bioinks in bioprinting may contain basic hydrogels. 37-41 decellularized matrix components, 42,43 microcarriers, 44,45 tissue spheroids 18,46 and strands, 47 cell pellets, 48 and/or some advanced bioinks such as multi-material bioinks, 49,50 interpenetrating network (IPN) bioinks, 51,52 nanocomposite bioinks^{53,54} and supramolecular bioinks.^{55,56} Hydrogels are the most prominent class of materials for bioinks because of their abilities to provide a viable microenvironment for the attachment, growth, and proliferation of cells.⁵⁷ Although defined in different ways, hydrogel generally refers to a water-swollen, and cross-linked polymeric network produced by the simple reaction of one or more monomers.⁵⁸ The cross-linked polymeric network in a hydrogel is capable of absorbing and retaining large quantities of water due to its hydrophilic functional groups attached to the polymeric backbone. 58,59 The structural integrity of hydrogels depends on cross-links formed between polymer chains via various chemical bonds and physical interactions. 60 Hydrogels have found numerous applications in bioprinting 21,22,24,50,61-63 due to their attractive features, such as their biocompatibility, 58,64 mechanical and structural similarity to the ECM of many tissues, 65 high permeability to oxygen, nutrients and other water-soluble compounds, ^{66,67} ability to be processed under relatively mild conditions, ⁶⁸ and porous flexible network enabling the migration and communication of embedded cells. 60,69-71

Generally, hydrogels can be classified into two groups: naturally derived, such as gelatin, collagen, chitosan, fibrin, silk fibroin, hyaluronic acid (HA), alginate, and agarose, and synthetically derived, such as poly(acrylic acid) (PAA) and its derivatives, poly(ethylene oxide) (PEO) and its copolymers, poly(vinyl alcohol) (PVA), polyphosphazene, and polypeptides. 41,68,72,73-78 In the past few decades, various hydrogels, blends of hydrogels, and cell-

laden hydrogels have been utilized as bioink components for bioprinting applications. Of course, not all bioinks are naturally printable for bioprinting applications.

Bioink printability is influenced by the rheological properties of bioinks, cross-linking mechanisms, and printing conditions. For the three major bioprinting technologies as mentioned previously, each has different printability requirements according to the printing mechanism employed. For example, inkjet printing is limited by the bioink viscosity while micro-extrusion can be used to print bioinks with a wide range of viscosity. Therefore, the bioink printability has been investigated for different bioprinting technologies in order to have a better control of the resulting printing quality and feature resolution. Phase diagrams have been constructed to present the bioink printability and provide a better understanding of the underlying physics during jet/droplet/filament formation processes during typical bioprinting. As such, it is desirable to investigate the bioink printability and related phase diagrams during different bioprinting processes in order to promote the wide adoption of bioprinting.

There has been a considerable amount of review work done regarding bioprinting techniques, 8,16,18,20,61,79-85 candidate biomaterials and/or biological materials used as bioinks, 36,37,59,60,68,76,86,87 and the applications of bioprinting. 4,34,88,89 However, the understanding of bioink printability is largely ignored, despite knowledge of bioink printability being crucial for the fabrication of complex living tissues with high shape fidelity. As a starting point, this complementary review presents a first-time comprehensive overview of bioink printability during direct bioprinting, which includes inkjet printing, laser printing, and micro-extrusion, while indirect bioprinting-related bioink printability studies are not covered herein.

It is noted that digital light processing (DLP) has also been implemented for the fabrication of cellular structures with micrometer resolution. 90-92 A typical DLP-based 3D bioprinter uses a digital micromirror array device to convert a 3D CAD model into a series of layered, 2D digital optical patterns for the photopolymerization of bioinks. 91 Due to its photopolymerization-based mechanism, common bioinks for DLP-based bioprinting are the mixtures of some functional elements, such as biomaterials, nanoparticles, and biomolecules, with biocompatible and photopolymerizable hydrogel precursors, such as gelatin methacrylate (GelMA). 90-92 Compared to the three main direct bioprinting techniques, bioinks are selectively cross-linked to fabricate 3D objects during DLP-based bioprinting instead of being transferred as filaments or droplets which are then deposited layer by layer to produce 3D tissue constructs. Generally, the main application of DLP-based 3D printing is for indirect bioprinting due to the difficulty in incorporating multiple types of living cells on demand during 3D printing and the intrinsically higher stiffness of materials suitable for DLP. Therefore, DLP-based 3D printing is not reviewed in this paper.

3. Evaluation of Bioink Printability

Under given printing conditions, a printable bioink is expected to have good thixotropic property and process-dependent shear thinning behavior, which enable the bioink to maintain a stable form at rest before printing but exhibit low viscosity when dispensed with a sufficient shear rate and regain its stability after printing. For example, Paxton *et al.*⁹³ proposed a two-step method for the assessment of the bioink printability during micro-extrusion bioprinting, focusing firstly on screening ink formulations to assess filament and droplet formation and the ability to form 3D

constructs and then presenting a method for the rheological evaluation of inks to characterize the vield point, shear thinning and recovery behavior (Figure 4).

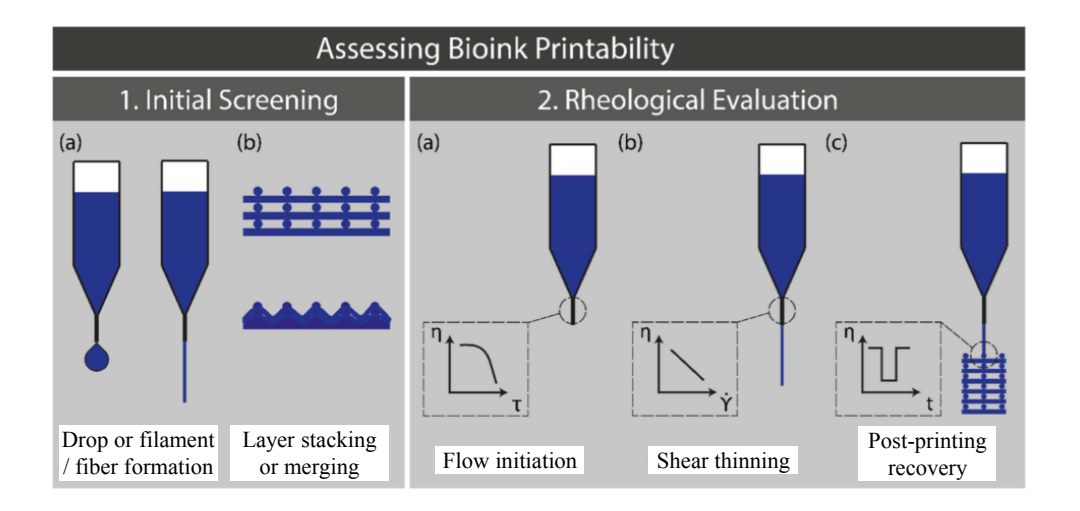


Figure 4. Outline of a proposed research method to assess the bioink printability during micro-extrusion. 1. Initial screening of ink formulations to establish (a) filament formation as opposed to droplet formation and (b) successful layer stacking without merging between layers. 2. Rheological evaluations are employed to characterize (a) the flow initiation properties and yield stress, (b) degree of shear thinning to predict the extrusion process and cell survival, and (c) recovery behavior of the inks after printing. Figures and captions are reproduced with permission from Biofabrication 9, 044107 (2017). Copyright 2017 IOP Publishing Ltd.

3.1. Typical time scales and dimensionless quantities for printability evaluation

During bioprinting, either droplet-based or filament-based, a small amount of bioink is ejected from a nozzle orifice during micro-extrusion and inkjet printing or a ribbon coating during laser printing to form a liquid jet. Then, the forming jet may maintain its shape to form a continuous bioink filament during micro-extrusion or break up into droplet(s) during inkjet printing or laser

printing due to hydrodynamic instability, which depends on printing conditions and bioink material properties. The jetting and droplet formation dynamics may be classified into different regimes based on the morphology and evolution of forming jets and droplets. The governing forces for jet formation and breakup, the dominant balance of forces, and the dynamics regimes during bioprinting should be rationalized and evaluated using system-specific dimensionless quantities.

In general, dimensionless quantities can be classified into two types: (1) dimensionless numbers, which are derived from any physical system using dimensional analysis. For the physical system investigated, the dimensionless numbers can be used to rationalize the dominant balance of forces depending on the relative magnitude of each physical effect in the system, and (2) dimensionless ratios, which are obtained by grouping and cancelling out the dimensions of certain system parameters of interest. In the following section, these two types of dimensionless quantities are introduced to evaluate the printability during bioprinting.

3.1.1 Dimensionless numbers for bioprinting

During bioprinting of viscoelastic bioinks, the jet formation, capillary thinning, and/or breakup of free surface liquid filaments can be characterized by three main time scales: visco-capillary time scale $t_v = \eta_0 R/\sigma$, inertio-capillary or Rayleigh time scale $t_c = \sqrt{\rho R^3/\sigma}$, and the longest relaxation time λ , where η_0 is the zero-shear viscosity, R is the characteristic length scale for the flow of interest which is usually taken as the radius of the nozzle orifice for the inkjet printing and laser spot radius for the laser printing, respectively, σ is the surface tension, ρ is the density, and λ is a characteristic time that relates to the motion of polymer chains. For most viscoelastic

bioinks, three material property-based dimensionless numbers can be derived based on the relative significance of these three time scales: the Ohnesorge number $Oh = \frac{t_v}{t_c} = \frac{\eta_0}{\sqrt{\rho\sigma R}}$, the elasto-capillary number $Ec = \frac{\lambda}{t_v} = \frac{\lambda\sigma}{\eta_0 R}$, and the intrinsic Deborah number $De_0 = \frac{\lambda}{t_c} = \sqrt{\frac{\lambda^2\sigma}{\rho R^3}}$. The Oh number represents the ratio of viscous to inertial effects, and the Ec or De_0 number represents the elastic to viscous or inertial effects, respectively. It should be pointed out that the Ec number is a Deborah number with a characteristic deformation time of t_v for viscous effect-dominated fluids instead of t_c . In addition, the Weber number $We = \frac{\rho R U^2}{\sigma}$, which represents the inertial to capillary effects, is usually introduced as a process dynamics-related dimensionless number to characterize the jetting dynamics, where U represents the characteristic velocity for the flow of interest. Some other dimensionless numbers commonly used in literature are the Reynolds number $Re = \frac{\rho UR}{n_0}$, which represents the ratio of inertial to viscous effects, the capillary number

 ${\rm Ca} = \frac{We}{Re} = \frac{\eta_0 U}{\sigma} \,, \ \, {\rm which \ represents \ the \ ratio \ of \ viscous \ to \ capillary \ effects, \ \, and \ \, Weissenberg}$ ${\rm number \ Wi} = \frac{\lambda U}{R} \,, \ \, {\rm which \ also \ represents \ the \ ratio \ of \ elastic \ to \ viscous \ effects.}^{94\text{-}96}$

For the breakup of Newtonian solutions, the elastic effects are negligible and their jetting dynamics can be conveniently captured by the Ohnesorge number (Oh) solely.⁹⁷ It is noted that the Ohnesorge number only depends on the thermophysical properties (viscosity, density, and surface tension) of fluids and the characteristic length scale of flows. In particular, a Z or J number, which is actually the inverse of the Ohnesorge number, ⁹⁸ has been extensively used for

the printability study during inkjet printing⁹⁹ and the jettability study during laser printing,¹⁰⁰ respectively. In addition, the Oldroyd number $Od = \frac{\tau_y d^n}{KU_{nozzle}}$, where U_{nozzle} is the print speed of the nozzle, d is the nozzle outer diameter, and K, n and τ_y are given by the Herschel-Bulkley equation, represents the ratio of the material yield stress to the viscous stresses in a flow and has been used to characterize the dimensions of the yielded areas of a Herschel-Bulkley fluid flowing around a cylinder.¹⁰¹ Table 1 further summarizes the aforementioned representative dimensionless numbers for bioprinting studies.

Table 1. Dimensionless numbers for bioprinting

Dimensionless	Definition	Physical interpretation
numbers		
Z or J number	$\sqrt{\rho\sigma R}$	The ratio of inertial to viscous effects
(Inverse of Oh	$oldsymbol{\eta}_{0}$	
number)		
Ohnesorge number	$\frac{\eta_0}{\sqrt{ ho\sigma R}}$	The ratio of viscous to inertial effects
(Oh)	$\sqrt{\rho\sigma}R$	
Elasto-capillary	$\frac{\lambda\sigma}{\eta_{_{0}}R}$	The ratio of elastic to viscous effects for flows with
number (Ec)	$\eta_{\scriptscriptstyle 0} R$	non-constant stretch history
Intrinsic Deborah	$\sqrt{\frac{\lambda^2 \sigma}{\rho R^3}}$	The ratio of elastic to inertial effects
number (De ₀)	$\sqrt{\rho R^3}$	
Weber number	ρRU^2	The ratio of inertial to capillary effects
(We)	σ	
Reynolds number	al ID	The ratio of inertial to viscous effects
-	$\left egin{array}{c} rac{ ho UR}{\eta_{\scriptscriptstyle 0}} \end{array} ight $	The fatto of mertial to viscous effects
(Re)		
Capillary number	$\frac{\eta_0 U}{\sigma}$	The ratio of viscous to capillary effects
(Ca)	-	
Weissenberg	$\frac{\lambda U}{R}$	The ratio of elastic to viscous effects for flow with
number (Wi)	K	constant stretch history
Oldroyd number	$\tau_y d^n$	Dimensions of the yielded areas of a Herschel-
(Od)	$KU_{nozzle}^{ n}$	Bulkley fluid flowing around a cylinder

3.1.2 Dimensionless ratios for bioprinting

In addition to the well-defined dimensionless numbers, which have clear physical meanings, different dimensionless ratios have been proposed to present their printability results in a generalized way. For example, a dimensionless ratio $\Pr = \frac{L^2}{16\,A}$, where L is the perimeter and A is the area of the cross-section of an extruded gelled bioink filament, has been proposed to quantify the circularity of printed filaments, which is then used to determine the gelation condition of the printed filaments. Similarly, a dimensionless ratio between the nozzle path speed and bioink dispensing velocity ($v = v_{path} / v_{out}$) has been proposed to represent the degree of adaptability between the dispensing speed and bioink feed rate and to evaluate the effects of operating conditions on filament formation during micro-extrusion printing. Since the elastic properties of both the support bath and bioink during micro-extrusion printing can affect the filament morphology, a material property-based dimensionless ratio, which is defined as the storage modulus ratio between the support bath and bioink: G'_{bath}/G'_{ink} has been utilized to assess the effects of material properties on filament formation. Table 2 gives the definition of some dimensionless ratios for bioprinting studies and their physical interpretation.

Table 2. Dimensionless ratios for bioprinting

Dimensionless ratios	Definition	Physical interpretation
Pr	$\frac{L^2}{16A}$	The circularity of the cross-
	16 A	section of printed filaments
Dispensing velocity ratio	v _{path} / v _{out}	The degree of adaptability
		between the dispensing speed
		and bioink feed rate
Storage modulus ratio	G'bath/G'ink	The effects of material
		properties on filament formation

3.2 Printability during droplet-based bioprinting

The printability and related phase diagrams during droplet-based printing are discussed in terms of inkjet printing and laser printing, respectively, as follows.

3.2.1 Printability during inkjet bioprinting

As a material jetting technique, inkjet printing offers various important advantages, including low cost, high resolution, high speed, and biocompatibility with many biomaterials and cells. Generally, inkjet printing is usually implemented in two main approaches: continuous inkjet (CIJ) printing and drop-on-demand (DOD) inkjet printing.¹⁰⁴ During CIJ printing, a liquid is forced under pressure through a small diameter orifice and the resulting jet spontaneously breaks up into a stream of droplets due to hydrodynamic instability. During DOD printing, droplets are generated only when required by propagating a pressure pulse in a fluid filled chamber, and the

pressure pulse is typically generated via either thermal expansion or piezoelectric actuation as shown in Figure 2a. Inkjetting has been widely implemented in various 1D and 2D patterning of Chinese hamster ovary (CHO) cells, ¹⁰⁵ bovine vascular endothelial cells, ¹⁰⁶ embryonic motoneuron cells, ¹⁰⁵ human NT2 neuronal precursor cells, ¹⁰⁷ HeLa cells, ¹⁰⁸ human fibroblasts ¹⁰⁹ and human adipose-derived stem cells, ¹¹⁰ to name a few. Inkjetting has also been pioneered to fabricate 3D cellular constructs such as vascular-like constructs. ^{21,24,111,112}

During a typical inkjet printing process, droplets are formed in air before they contact a receiving substrate. The printability of different materials including Newtonian materials, non-Newtonian materials, and cell-laden bioinks during inkjet printing has been of long-standing interest to the printing research and development community. For Newtonian materials, Dong et al. 113 systematically investigated the main droplet formation stages during DOD inkiet printing of water and glycerol-water solutions, and reported that a typical process of successful droplet formation usually consists of liquid ejection and stretching, breakup/pinch-off, contraction and breakup of liquid threads, and recombination of primary and satellite droplets as shown in Figure 5. They also reported two modes of breakup after the free liquid thread pinch-off from the nozzle exit depending on the operating conditions: end-pinching where the liquid thread pinches off from an almost spherical head (Figure 5a), and multiple breakups due to capillary waves (Figure 5b). Jang et al. 99 studied the inkjetting printability when using Newtonian glycerol-water solutions with different rheological properties and reported that the printability of Newtonian fluids during inkjet printing is determined by the inverse of the Ohnesorge number, which is a function of viscosity, surface tension, and density of the ink fluids. For non-Newtonian materials, Yan et al. 114 investigated the droplet formation process of polyethylene oxide (PEO) solutions

during inkjet printing and concluded that either the increasing PEO molecular weight or the increasing concentration has a significant effect on the droplet formation process, by increasing the breakup time, decreasing the primary droplet speed, and decreasing the number of satellite droplets. Hoath *et al.*⁹⁶ studied the jetting behavior of dilute polymer solutions during inkjet printing and presented a quantitative model to predict three different regimes depending on the jet Weissenberg number (Wi) and the extensibility of the polymer molecules. Xu *et al.*¹¹⁵ further classified four breakup types (as shown in Figure 6), namely front pinching (Figure 6a), hybrid pinching (Figure 6b), exit pinching (Figure 6c), and middle pinching (Figure 6d), based on the first pinch-off location during inkjet printing of viscoelastic alginate solutions. In particular, front pinching is mainly governed by a balance of inertial and capillary effects, exit pinching is affected by the external actuation-induced hydrodynamic instability and mainly governed by a balance of elastic and capillary effects, middle pinching usually occurs any place along a uniform thin ligament under dominant viscous and elastic effects, and hybrid pinching happens when front pinching and exit pinching occur simultaneously as a special case.

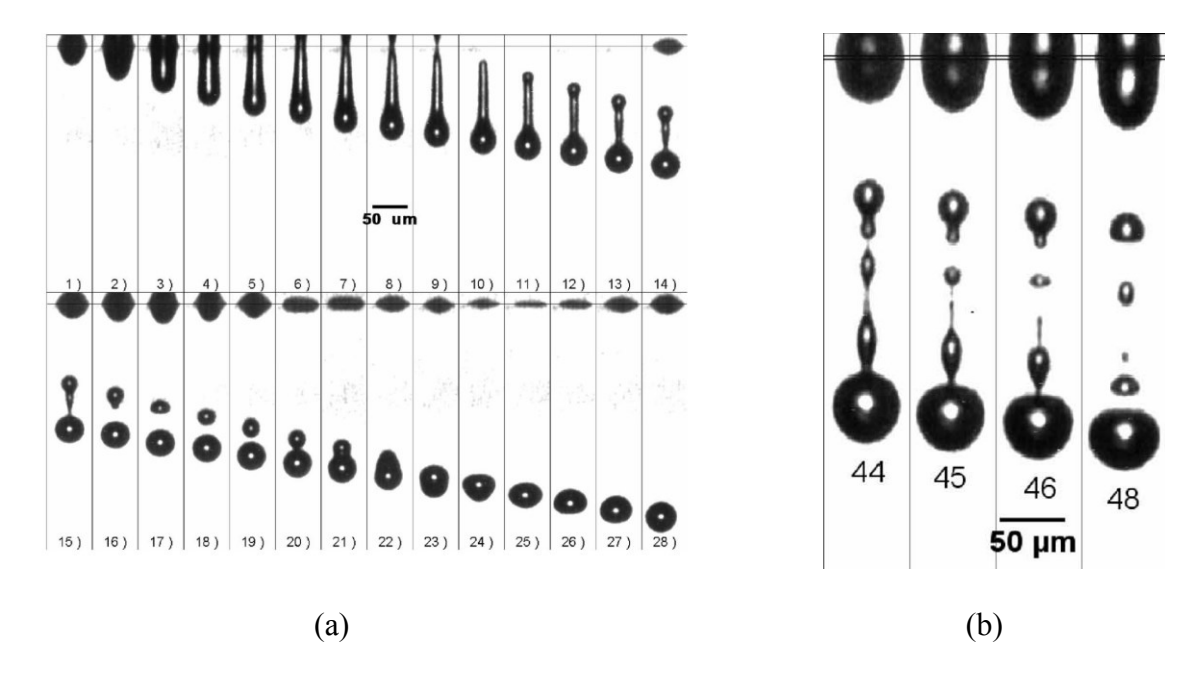


Figure 5. (a) Representative images of successful droplet formation process during DOD inkjet printing of Newtonian glycerol solutions, and (b) multiple breakups of a free liquid thread after it pinches off from the nozzle. Figures and captions are reproduced with permission from Physics of Fluids 18, 072102 (2006). Copyright 2006 American Institute of Physics.

The addition of living cells to bioinks forms soft particle-laden suspensions. For 3T3 fibroblast-laden alginate/DMEM bioinks, Xu *et al.*¹¹⁶ systematically investigated the effects of cell concentration on the droplet formation process during inkjet printing of cell-laden bioinks in terms of the breakup time, droplet size and velocity, and satellite droplet formation. Furthermore, the cell-laden droplet formation process was compared with that during inkjet printing of a comparable polystyrene microbead-laden suspension under the identical operating conditions to understand the effect of particle physical properties on the droplet formation process. As reported, when the cell concentration of bioink increases, the droplet size and velocity decrease, the formation of satellite droplets is suppressed, and the breakup time increases; when

comparing with a hard bead (polystyrene)-laden suspension, the cell-laden bioink has a smaller ejected fluid volume, lower droplet velocity, and longer breakup time. Zhang *et al.*¹¹⁷ further classified two types of ligament flows based on the flow direction at the locations near the nozzle orifice and the forming droplet during inkjet printing of 3T3 fibroblast-laden alginate/DMEM bioinks: one with different flow directions and the other with the same flow direction. The effects of ligament flow on the cell distribution and cell viability were studied, and it was reported that fewer cells are ejected with the primary droplet during the former scenario because some cells in the ligament are driven back into the nozzle by the retracting flow.

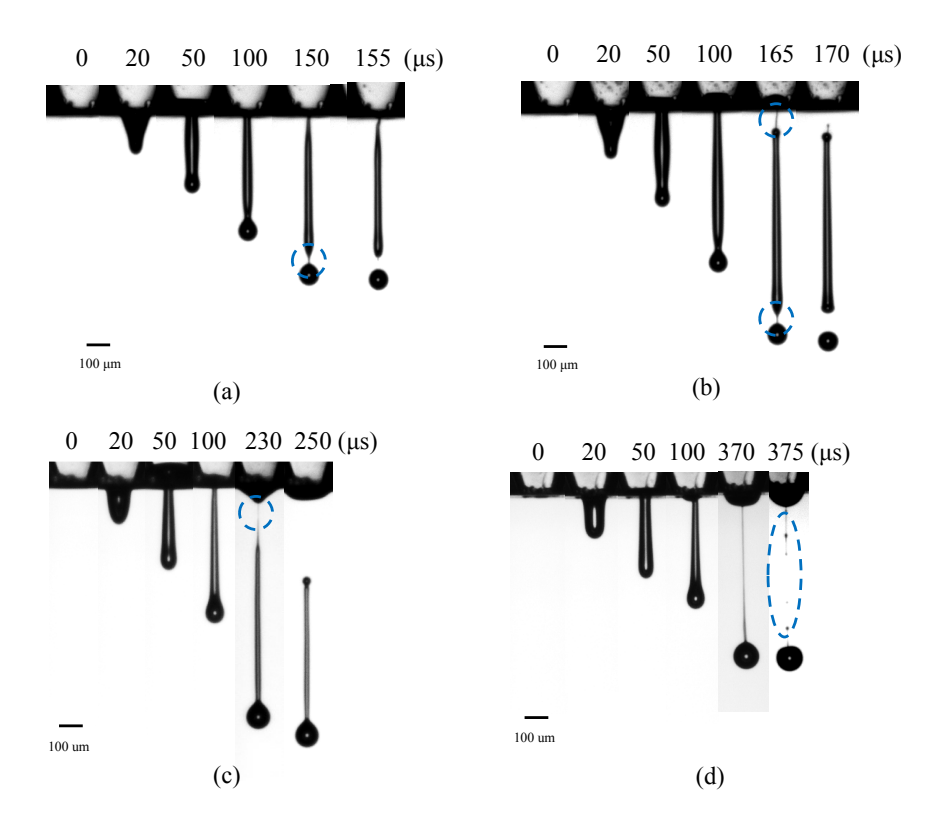


Figure 6. Four pinch-off types during DOD printing of alginate solutions: (a) front pinching, (b) hybrid pinching, (c) exit pinching, and (d) middle pinching. Sodium alginate concentration and excitation voltage are listed as follows: (a) 0.30% and 35 V, (b) 0.30% and 42 V, (c) 1.00% and 50 V, and (d) 2.00% and 50 V. Each pinch-off location is highlighted using a dashed circle. Figures and captions are reproduced with permission from Langmuir 33, 5037 (2017). Copyright 2017 American Chemical Society.

3.2.2 Printability during laser bioprinting

Laser bioprinting (Figure 2b), a versatile laser-induced forward transfer-based technique, ^{82,118,119} has emerged as a promising orifice-free direct-write strategy for bioprinting. During a typical laser bioprinting process, bioink is prepared as a thin-film coating on the bottom side of a light

transparent quartz support, which together form a ribbon. Laser pulses, usually ultraviolet (UV), are then guided to pass through the top side of the ribbon perpendicularly and focus on the interface between the quartz support and the thin-film coating. The laser-matter interaction generates localized heat to sublime a small portion of the coating to form a high-temperature, high-pressure vapor bubble. The consequential bubble expansion then propels part of the bioink coating away from the ribbon, resulting in different types of jets/droplets as shown in Figure 7, and the forming jets/droplets then impinge onto the receiving substrate to generate droplet(s) with different morphological properties as shown in Figure 8. The generated droplets are building blocks for biofabrication.

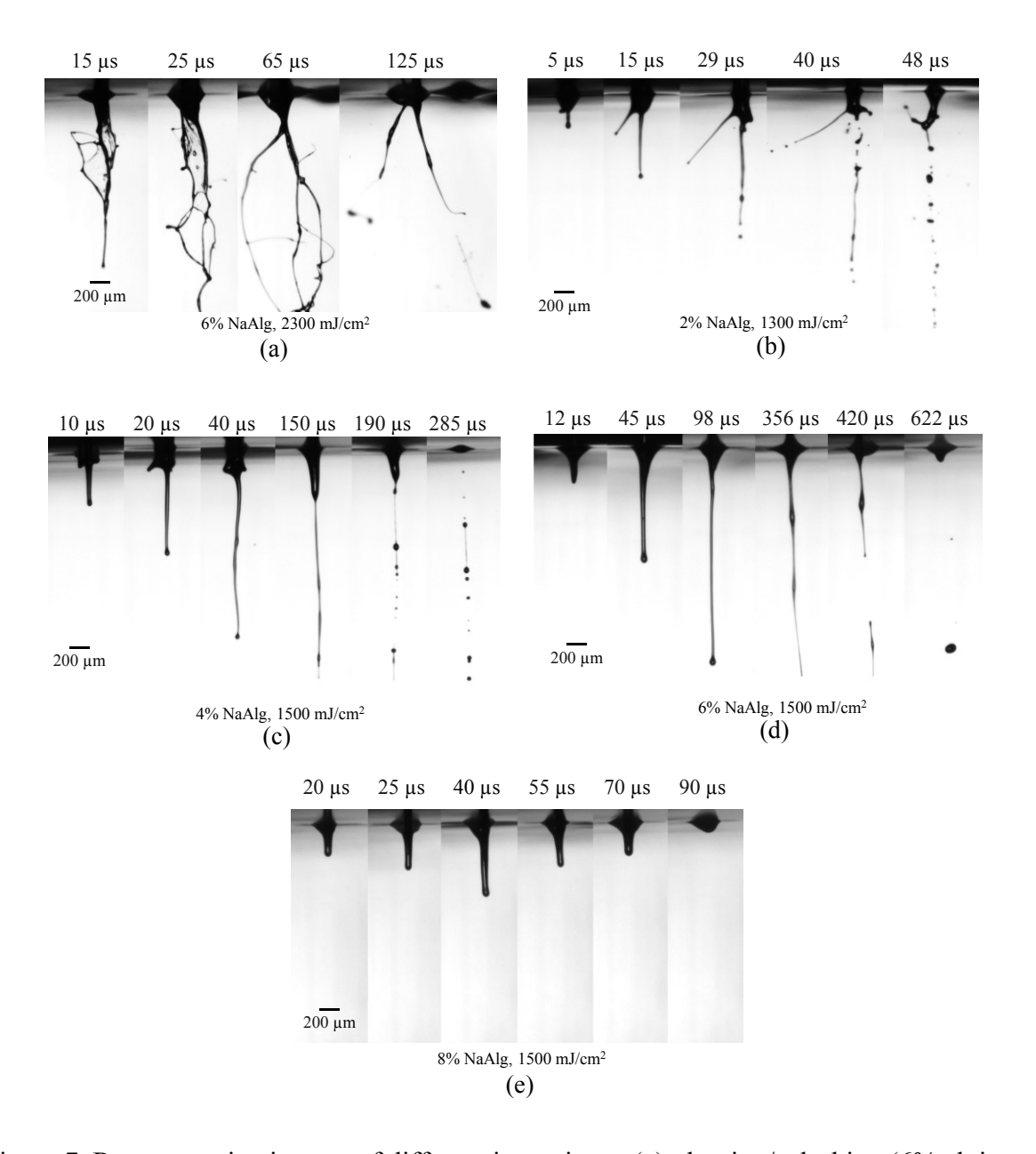


Figure 7. Representative images of different jet regimes: (a) pluming/splashing (6% alginate, 2300 mJ/cm²), (b) jetting with a bulgy shape (2% alginate, 1300 mJ/cm²), (c) well-defined jetting with an initial bulgy shape (4% alginate, 1500 mJ/cm²), (d) well-defined jetting (6% alginate, 1500 mJ/cm²), and (e) no material transferring (8% alginate, 1300 mJ/cm²). Figures and captions are reproduced with permission from Langmuir, **31**, 6447 (2015). Copyright 2015

American Chemical Society.

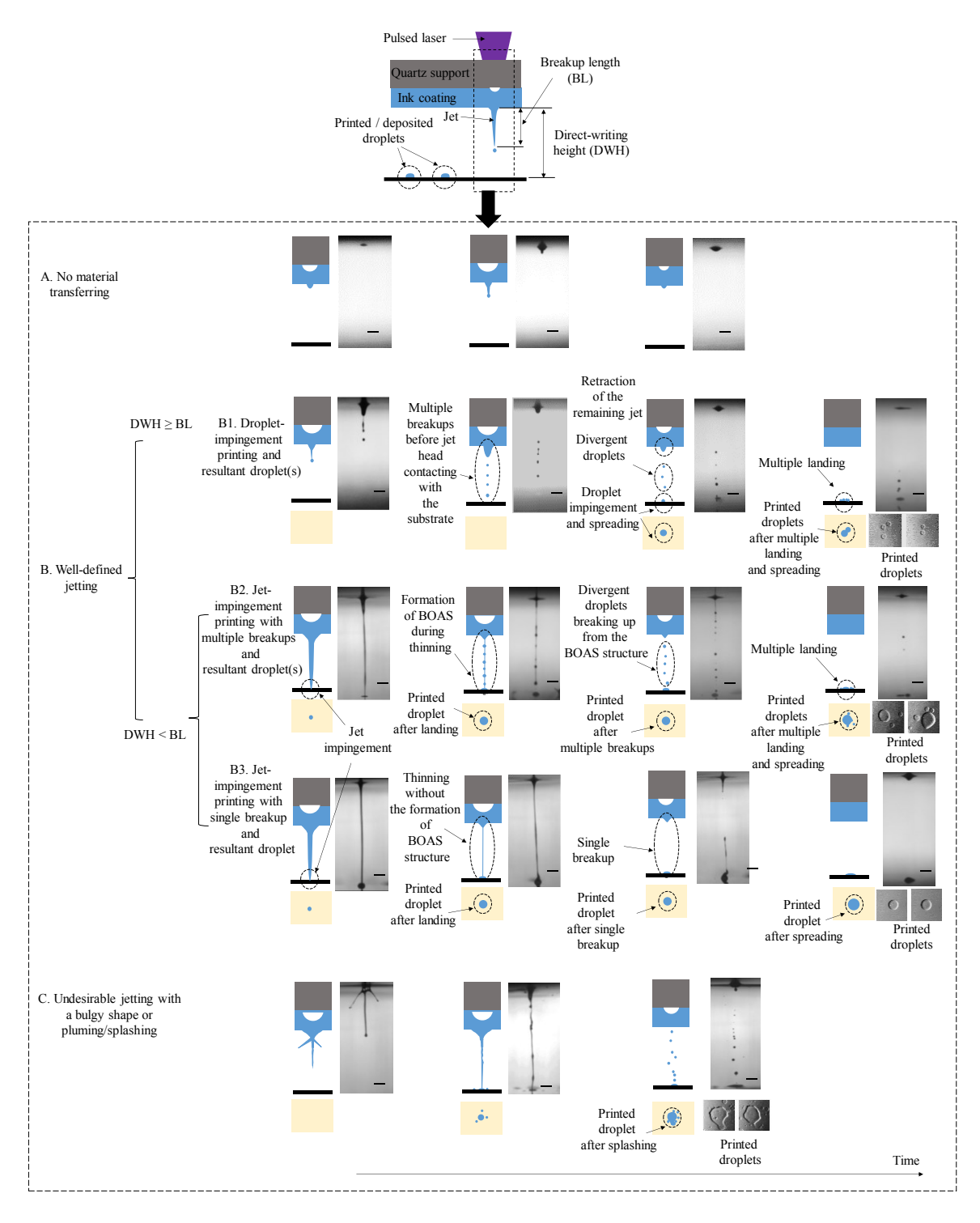


Figure 8. Schematics of material deposition dynamics and representative images under different alginate concentrations and operating conditions. The direct-writing height was 2.0 mm. The scale bars: 200 µm. ¹²² Figures and captions are reproduced with permission from Langmuir, **32**, 3004 (2016). Copyright 2016 American Chemical Society.

The printing resolution is usually evaluated based on the size and shape of printed droplets, which are influenced by the rheological properties and thickness of the bioink coating, the laser fluence, the direct-writing height, and the wettability of the receiving substrate. Because of its orifice-free nature, laser bioprinting can handle a wide range of bioinks without suffering from the possible clogging, material compatibility, and contamination issues typically associated with other nozzle-based bioprinting techniques such as inkjet printing. As such, laser bioprinting has been widely adopted to print different biomaterials as well as biological materials, such as hydrogels, 22,121,122,124 peptides, 125 DNA, 126 and living cells, 127-132 to name a few. Furthermore, both acellular and cellular constructs have been successfully fabricated in 2D and/or 3D by laser bioprinting. 22,124,132

Laser printing usually results in a jet with a much higher jet velocity (on the order of 10 m/s) than that during inkjet printing (on the order of 1 m/s) due to their different working mechanisms. It is less likely for laser printing to generate a single droplet in air as happens during a typical inkjet printing process. Instead, a long thin jet is formed and then impinges onto the receiving substrate to transfer the materials during laser printing as illustrated in Figure 8, and the size and morphology of printed droplets are mainly determined by the jet/droplet formation and jet/droplet impingement and deposition processes. Instead, a long thin jet is formed and then impinges onto the size and morphology of printed droplets are mainly determined by the jet/droplet formation and jet/droplet impingement and deposition processes. Instead, a long thin jet/droplet formation from the instead of the printing as illustrated in Figure 8, and the size and morphology of printed droplets are mainly determined by the jet/droplet formation from the impingement and deposition processes. Instead, a long thin jet/droplet formation from the instead of the printing that it is formed and then impinges onto the receiving substrate in Figure 8, and the size and morphology of printed droplets are mainly determined by the jet/droplet formation from the printing from the printing

studied to have a better understanding of the printability of bioinks to fully realize the potential of laser printing.

The jet/droplet formation process, in particular, has been investigated during the laser printing of various bioinks, such as Newtonian glycerol-based solutions, 100,141 viscoelastic alginate solutions, ^{121,143} and cell-laden alginate suspensions. ¹³³ For Newtonian glycerol-based solutions, three main jetting regimes have been identified during the jet/droplet formation process: (1) no material transferring, in which no material is transferred, (2) well-defined jetting, in which welldefined jetting/droplets may be obtained, and (3) jetting with a bulgy shape/pluming/splashing, in which satellite droplets may appear. 100,141 For viscoelastic alginate solutions, there is a unique jetting regime in addition to the three regimes as mentioned above, during which a jet with an initial bulgy shape may develop into a well-defined jet. 121 The jet/droplet deposition process has also been investigated for Newtonian glycerol-based solutions, 134 viscoelastic alginate solutions, 122 and cell-laden alginate suspensions. 133 For glycerol-based solutions, the formation of single droplets on a receiving substrate is mainly due to the contact of ejected liquid jets with the receiving substrate. 134 For viscoelastic alginate solutions, the deposition process has been classified into three types for the well-defined jetting regime based on the jet/droplet impingement types (Figure 8): (1) droplet-impingement printing, (2) jet-impingement printing with a single breakup, and (3) jet-impingement printing with multiple breakups. 122 Of these, the best printing quality is achieved with single breakup jet-impingement printing, while dropletimpingement printing produces the lowest quality printing; the printing quality can be improved by using high-concentration alginate solutions and/or decreasing the direct-writing height. 122 However, the laser fluence selection is a compromised decision. Compared with those during

cell-free bioink printing, the transfer threshold is higher, but the jet velocity is lower, the jet breakup length is shorter, and printed droplet size is smaller during laser printing of 3T3 fibroblast-laden alginate/DMEM bioinks.¹³³ The addition of living cells transforms the printing type from jet-impingement printing to droplet-impingement printing. Non-ideal jetting behaviors have been observed, which might be attributed to the local nonuniformity and nonhomogeneity of cell-laden bioinks.¹³³

3.2.3 Phase diagrams

As droplet-based bioprinting technologies, inkjet and laser printing produce droplets on demand, which are utilized as building blocks for biofabrication. The dynamics of droplet formation is determined by operating conditions and material properties of bioinks. In practical applications, optimal combinations of operating conditions and bioink material properties are often selected by trial and error to ensure good printability. However, such a selection process is often tedious and time-consuming if a practitioner does not have a holistic understanding of the dynamics of a given droplet-based bioprinting process. As such, phase or operability diagrams have been studied to provide not only the knowledge of optimal operating conditions but also the information on adversarial conditions to be avoided.¹⁴⁴⁻¹⁴⁹

A typical phase diagram is constructed based on operating parameters, material property-based dimensionless numbers, process dynamics-related dimensionless numbers, and/or a combination of these to show conditions for distinct modes to occur. Phase diagrams can also service as databases for researchers to add and/or exchange existing experimental and/or numerical results. Different phase diagrams have been constructed related to the breakup of liquid filaments of

dripping faucets^{94,145,146} and the formation of beads-on-a-string (BOAS) structures on a liquid bridge,¹⁵⁰ to name a few. Similarly, phase diagrams (and operability diagrams) have also been constructed to study the printability of different bioinks during inkjet and laser printing.

3.2.3.1 Inkjet bioprinting phase diagram

For phase diagrams during inkjet bioprinting of Newtonian materials, the common dimensionless numbers are the inverse Ohnesorge number (usually as Z and J numbers), Weber number (We), and capillary number (Ca). Z number was proposed to determine the printability during inkjet printing of Newtonian materials, and the printable range was identified as $4 \le Z \le 14$ by considering the single droplet formability, positional accuracy, and maximum allowable jetting frequency. 99 Printing using a fluid with a low Z value (less than 4) results in droplet formation with a long-lasting ligament (Figure 9a and 9b), which degrades the positional accuracy and printing resolution; printing using a fluid with a high Z value (above 14) results in undesirable satellite droplets due to large kinetic energy and high surface tension (Figure 9c). As shown in Figure 9d, a similar phase diagram was also proposed based on the Z number, Weber number, and Reynolds number (Re) for a large range of fluid properties with particle-filled inks. 144,147 The effects of dimensionless numbers on the droplet formation dynamics and printability range during inkjet printing of Newtonian materials were numerically investigated, and five regimes of droplet formation behavior were classified.⁹⁵ In Regime I, a single droplet is formed due to the absence of second pinch-off or recombination of satellite droplets with the primary droplet. In Regime II, Ca is small and We is large. One or more satellite droplets are generated, but they do not recombine with the primary droplet. In Regime III, both Ca and We are large. After a relatively longer pinch-off time, very thin and long-lasting threads break into fine satellite

droplets, which are not merged with the primary droplet due to a larger deceleration from air drag. In Regime IV, Ca is large and We is small, and the fluid fails to eject because the high viscous force dissipates the inertial force required to eject the fluid out of the nozzle. In Regime V, both Ca and We are small, and the fluid fails to eject because the large surface tension resists fluid ejection.

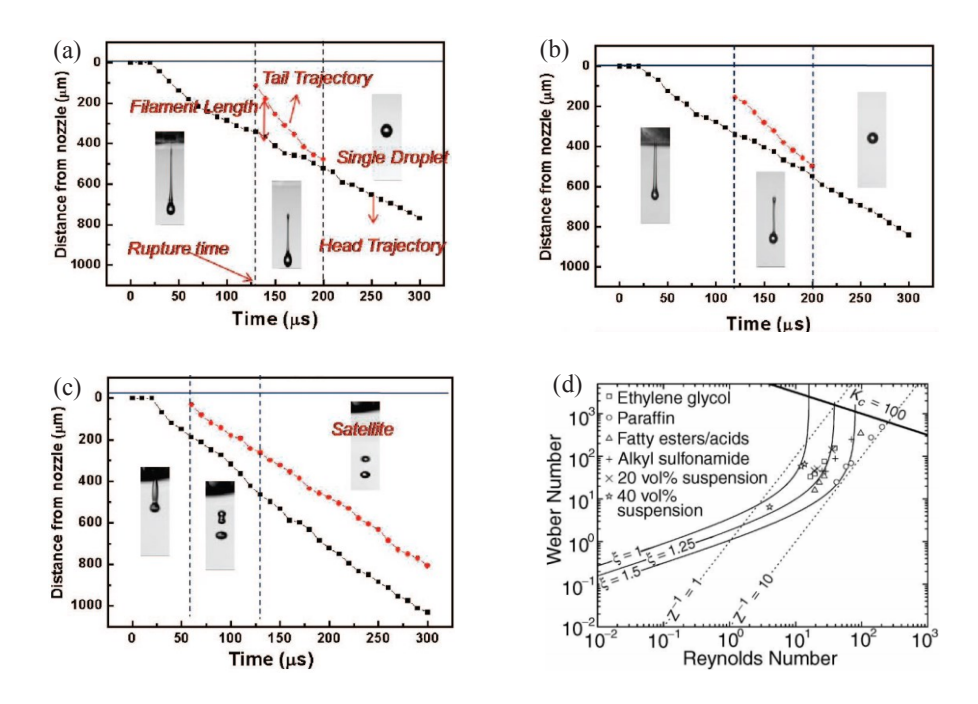


Figure 9. Representative trajectories of the ejected droplets as a function of elapsed time for fluids with values of Z: (a) Z=2.17, (b) Z=3.57, and (c) Z=17.32.⁹⁹ (d) Example phase diagram during DOD inkjet printing of particle-filled inks.¹⁴⁴ Figures and captions are reproduced with permission from (1) Langmuir, **25**, 2629 (2009). Copyright 2009 American Chemical Society and (2) MRS Bulletin **28**, 815 (2003). Copyright 2003 Materials Research Society.

For phase diagrams during inkjet bioprinting of non-Newtonian materials, the common dimensionless numbers are Weissenberg number (Wi) and Deborah number (De). Hoath *et al.* ⁹⁶

presented a quantitative model to predict three different regimes of behavior during inkjet printing of viscoelastic materials depending on Wi and the polymer chain extensibility L. In Regime I (Wi < 1/2), the polymer chains are relaxed and the fluid behaves in a Newtonian manner. In Regime II (1/2 < Wi < L), the fluid is viscoelastic, but the chains do not reach their extensibility limit. In Regime III (Wi > L), the chains remain fully extended in the thinning ligament. The maximum polymer concentration at which a jet with a certain speed can be formed scales with the molecular weight to the power of 1-3v, 1-6v, and -2v in the three regimes, respectively, where v is the solvent quality coefficient. Morrison et al. 151 numerically investigated the effects of viscoelastic parameters (polymer concentration, De, and polymer chain extensibility) on the droplet formation process during inkjet printing of viscoelastic materials. Six jet behaviors were classified: single droplet, Newtonian, fewer (larger) satellites, beads-on-a-string, some tail retraction, and bungee. Single droplet regime happens only at small polymer chain extensibility, while beads-on-a-string regime only exists at relatively large values of the polymer chain extensibility. For De << 1, the fluid is only weakly elastic and the jet breakup is Newtonian in character. For De > 1, the type of jet behaviors for a given polymer chain extensibility is determined mainly by the polymer concentration.

3.2.3.2 Laser bioprinting phase diagram

The printability during laser printing was investigated during the jet/droplet formation process^{100,121} and the jet/droplet impingement and deposition process,¹²² respectively. Accordingly, the phase diagrams corresponding to the two processes were constructed to study the dynamics of the droplet formation during laser printing.^{121,122} For the phase diagram during the jet/droplet formation process of Newtonian fluids, a dimensionless number J was proposed

(the same as the Z number in the inkjet printability study), which is the inverse of the Ohnesorge number (Oh), to study the jet formation process. 100 The proposed J number, laser fluence, and glycerol concentration were employed to distinguish different jet forming regimes during the laser printing of glycerol-water solutions with different glycerol concentrations. 100 It is observed that a good jet forms at $0.09 \le J \le 1.76$ (corresponding to 75% to 85%) under the laser fluence of 717 mJ/cm². Figure 10 illustrates different jetting regimes (no materials transferred, good jet forming, and splashing/bulgy) delineated using dashed lines based on the experimental observations as the laser fluence varies. 100 Figure 10a is based on the laser fluence and jettability number, J, while Figure 10b is based on the laser fluence and glycerol concentration.

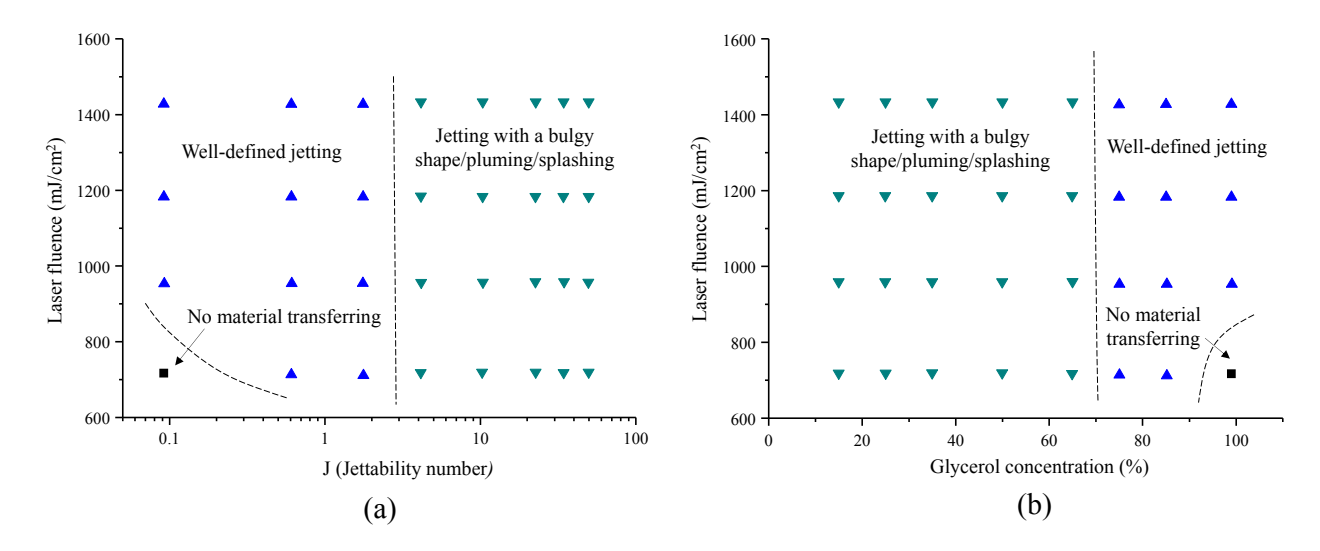


Figure 10. The influence of glycerol concentration and laser fluence on the jet morphology and printability (Dashed lines are for illustration only). Figures and captions are reproduced with permission from Journal of Applied Physics, **112**, 083105 (2012). Copyright 2012 American Institute of Physics.

For the phase diagram during the jet/droplet formation process of non-Newtonian fluids such as alginate solutions, the jetting regimes can be mapped out in a 3D phase diagram in a (We, Ec,

Oh) space as shown in Figure 11a by considering the contributions from both the process dynamics (We) and the material properties (Ec and Oh). For further illustration, four We number-defined planes in (We, Oh) and (We, Ec) spaces are drawn as mid-planes to distinguish two nearby jetting regimes as seen in Figure 11b and c. These two phase diagrams show five distinct jet formation regimes in both the (We, Oh) and (We, Ec) spaces. As the We number increases, the jetting behavior changes from no material transfer to well-defined jetting to well-defined jetting with an initial bulgy shape to jetting with a bulgy shape to pluming/splashing for both phase diagrams. As the Oh number increases or the Ec number decreases, which represents an increasing polymer concentration, the We number required for the jetting regime switch increases accordingly. For a given We number, increasing viscous and/or elastic effects help stabilize jetting or even suppress the formation of jets as seen from Figure 11d, which illustrates the effects of material properties in a (Oh, Ec) space.

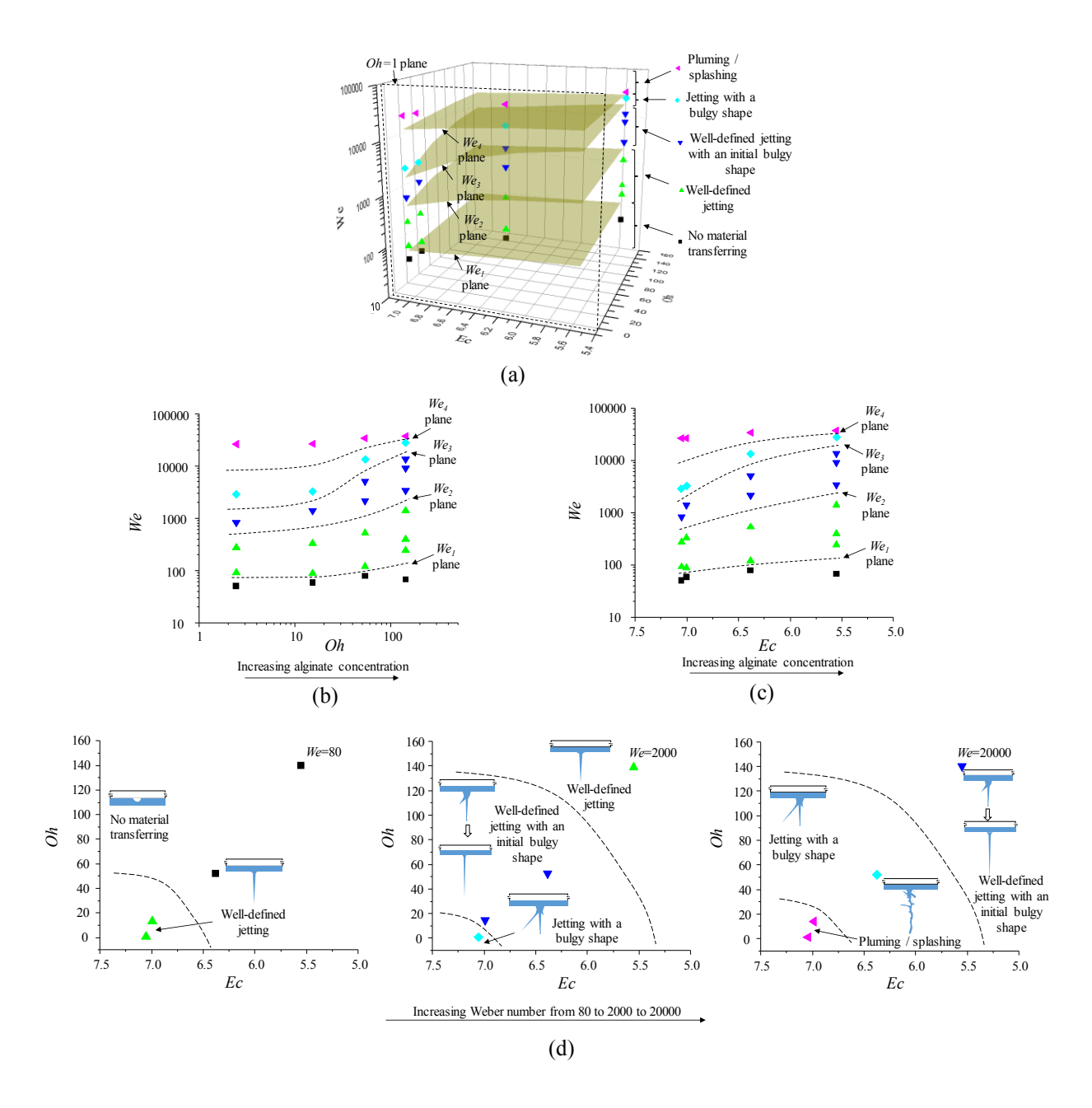


Figure 11. Jetting regime as a function of a) We, Oh, and Ec numbers, b) We and Oh numbers, c) We and Ec numbers, and d) Oh and Ec numbers. Figures and captions are reproduced with permission from Langmuir, **31**, 6447 (2015). Copyright 2015 American Chemical Society.

For the phase diagram during the droplet impingement and deposition process of non-Newtonian fluids, the three printing types for the well-defined jetting regimes¹²² can be further mapped out

in two (We, Oh) and (We, Ec) phase diagrams, respectively. ¹²² As shown in Figure 10, they were derived from the 3D (We, Oh, and Ec) space proposed for the laser printing of viscoelastic alginate solutions. ¹²² The dashed lines in Figure 12 separate the droplet-impingement printing, jet-impingement printing with multiple breakups, and jet-impingement printing with single breakup regimes from each other, and they are for illustration only based on the applicable experimental data.

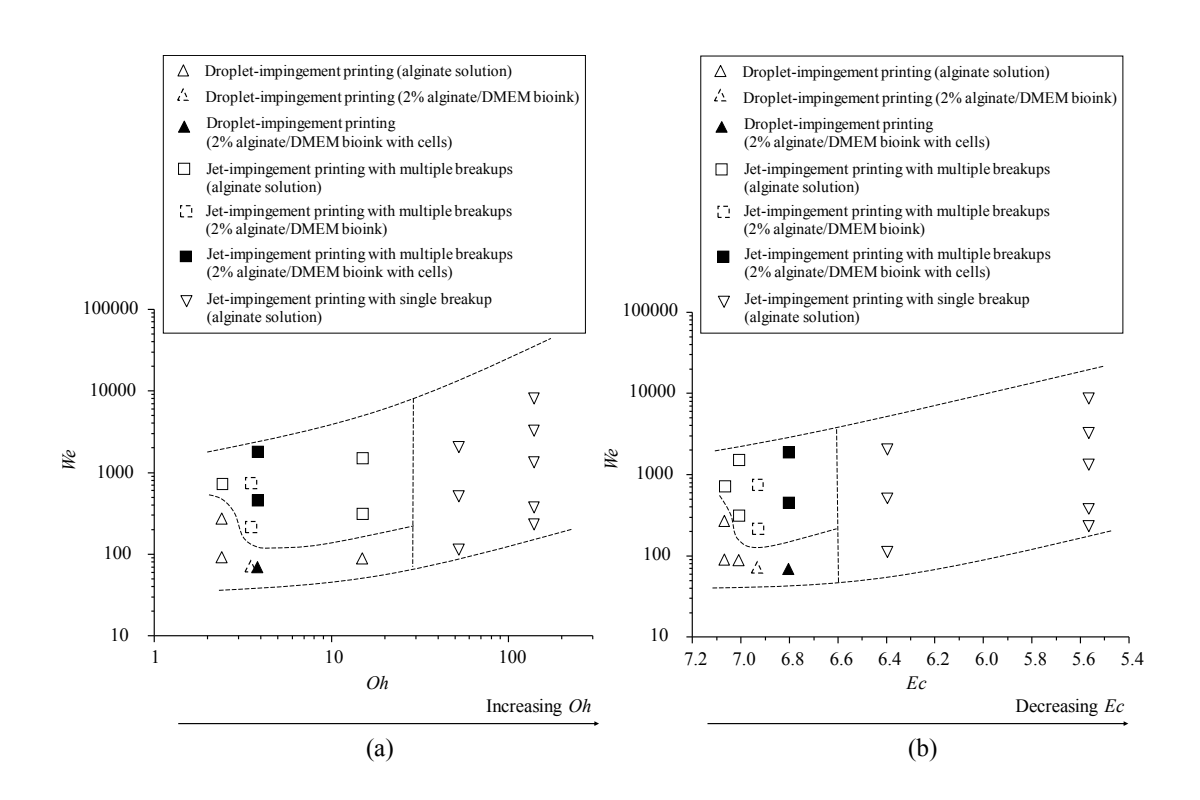


Figure 12. Printing type: (a) as a function of We and Oh numbers and (b) as a function of We and Ec numbers. Figures and captions are reproduced with permission from Biomicrofluidics 11, 034120 (2017). Copyright 2017 AIP Publishing.

Zhang et al. 133 further investigated the effects of living cells on the bioink printability during laser printing, in which NIH 3T3 fibroblast-free alginate/Dulbecco's Modified Eagles Medium

(DMEM) and 3T3 fibroblast-laden alginate/DMEM bioinks were printed. The printability of the cell-laden bioinks was mapped in the same two (We, Oh) and (We, Ec) phase diagrams as during the laser printing of non-Newtonian fluids. As seen from Figure 12, the delineation of different printing types is similar based on the two phase diagrams of the cell-free alginate, cell-free alginate/DMEM, and cell-laden alginate/DMEM bioinks, indicating that the effects of DMEM and living cells on the bioink printability can be sufficiently captured by the material propertyrelated dimensionless numbers (Oh and Ec). This in turn supports the effectiveness of these phase diagrams. Generally, for given Oh or Ec numbers, as the We number increases, the printing type changes from droplet-impingement printing to jet-impingement printing with multiple breakups. At high Oh or low Ec numbers, representing high alginate concentrations, the formation of BOAS structures is suppressed. As a result, the printing type remains jetimpingement printing with single breakup. For a given We number, the printing type may change from droplet-impingement printing to jet-impingement printing with multiple breakups to jetimpingement printing with single breakup as the Oh number increases or the Ec number decreases, which reflects the scenario of an increasing alginate concentration or the addition of living cells.

3.3 Printability during filament-based bioprinting

As one of the most explored and affordable bioprinting techniques, micro-extrusion bioprinting as shown in Figure 2c provides a powerful tool for the precise deposition of biomaterials and living cells by extruding continuous cylindrical filaments into 3D custom-designed structures. A pneumatic or mechanical (piston or screw-based) dispenser is generally used for bioink dispensing. The pneumatic-driven system can dispense various types of bioinks with a wide

range of viscosity by controlling the pressure and valve gating time while the mechanically-driven system may provide more direct control over the bioink flow, leading to more accurate spatial control. Various bioink types can be printed including hydrogels and hydrogel composites, 50,103,153-157 decellularized matrix components, 158,159 tissue spheroids, 47,160 and cell pellets. In addition, the high throughput during micro-extrusion bioprinting allows easy scale-up biofabrication of a wide variety of tissue constructs including but not limited to skin, 161 bone, 162 cartilage and menisci, 163,164 heart valves, 165,166 blood vessels, 167 and nerves. 168

3.3.1. Printability during micro-extrusion bioprinting

During filament-based micro-extrusion, two approaches are widely investigated and utilized including self-supporting *in situ* rapid solidification and support bath-enabled fabrication. For the former approach, different stimuli are introduced to induce rapid solidification of deposited structures *in situ*, while for the latter approach, deposited structures are usually printed and supported in a support bath and cross-linked during and/or after printing.¹⁵⁴

Bioink printability investigations during self-supporting rapid solidification printing have mainly focused on the effects of several key factors, including the bioink rheological properties, ^{49,87,156,169-171} bioink compositions, ¹⁷²⁻¹⁷⁵ and operating conditions. ^{165,176,177} In particular, the extrudability has been studied based on the droplet/filament formation behavior ^{93,178-181} as shown in Figure 13a and size, ^{177,181} and formability has been investigated based on the printing resolution, ^{171,174,177,182} shape fidelity ^{165,181,183} as shown in Figure 13b, and post-printing stability ^{93,173,179} of bioinks. Among these factors, the rheological properties and compositions of bioinks mainly affect the filament morphology, shape fidelity, and post-printing

stability. A suitable viscosity range can help form continuous filaments during extrusion and provide good shape fidelity after deposition. 174,176,184

Different methods have been adopted to modify the rheological properties of bioinks. For example, Chung *et al.*⁴⁹ mixed gelatin with sodium alginate to prepare an interpenetrating network (IPN) bioink for better printability. The extruded filaments have well-defined morphology and a controllable diameter, resulting in printed parts with better resolution. Mouser *et al.*¹⁷⁹ added gellan into gelatin methacrylate (GelMA) to improve filament deposition by inducing yielding behavior. Jin *et al.*¹⁸¹ used nanoclay as an internal scaffold material to mix with hydrogel precursors for printing-in-air applications. The resulting nanocomposite hydrogels have the yield-stress property which can effectively improve the extrudability and formability. Operating conditions usually determine the filament size and printing resolution. Some operating parameters including the nozzle diameter, dispensing pressure, standoff distance/path height, step distance/path space, and print speed (nozzle speed) can affect the filament width and printing resolution of 3D structures significantly. Generally, smaller filament width and higher printing resolution can be achieved by decreasing the nozzle diameter and dispensing pressure while increasing the standoff distance and print speed. Generally

Support bath-enabled bioprinting is an emerging extrusion-based 3D printing strategy, in which 3D structures are printed directly in a support bath while retaining their shapes. ^{50,55,154,185-188} Since the support bath can hold the printed structures stably *in situ*, it is unnecessary to rapidly solidify the printed 3D structures. Instead, they can be either gradually cross-linked during printing ^{55,185-188} or simultaneously cross-linked after printing. ^{50,154,155} Thus, the filament

formation during support bath-enabled bioprinting is in a liquid-in-liquid environment, and the effects of surface tension along the liquid-air interface and gravitational force are minimized during printing.

Bioink printability investigations in the support bath-enabled printing approach are similar to those in the self-supporting rapid solidification approach, while focusing more on the effects of support bath materials on the bioink filament formation. For example, Hinton et al. 187 printed PDMS filaments in support baths with different graded Carbopol suspensions. Both Carbopol 940 and ETD 2020 can produce smooth, cylindrical filaments while Carbopol Ultrez 30 can only produce filaments with a rough surface. Jin et al. 103 systemically investigated the filament formation of alginate-gelatin blends in nanoclay support baths. By varying the combination of material properties and operating conditions, seven filament types as shown in Figure 13c are possible during extrusion printing in the nanoclay bath including three types of well-defined filaments (swelling filament, equivalent diameter filament, and stretched filament) and four types of irregular filaments (rough surface filament, over-deposited filament, compressed filament, and discontinuous filament). It should be pointed out that while this filament classification study 103 was based on the support bath-based process, the resulting knowledge also applies to the selfsupporting rapid solidification micro-extrusion process. The formation of a good filament is influenced by the material properties in the form of the Plateau–Rayleigh instability. 189 Muth et al. 190 found that for support bath-enabled printing, the ink and bath materials must meet several requirements: 1) the inks possess a shear elastic modulus and yield stress which are approximately an order of magnitude larger than those of the support bath materials, 2) the support bath materials must possess a sufficiently high elastic modulus to support the printed

structures and an appropriate yield stress which allows the nozzle to move freely in the bath as well as prevents the disturbance of nozzle movement on the deposited features, and 3) the ink and support bath materials should be chemically compatible.

Since the micro-extrusion process is a slowly dispensing process and doesn't intentionally encourage the occurrence of breakups, jetting is usually avoided and the non-ideal jetting behaviors are not of interest as during the droplet-based processes. The deposited cellular filaments and extrusion printability are not specifically investigated since the local nonuniformity and nonhomogeneity of living cells don't significantly alter the macroscopic material properties of cell-laden bioinks.

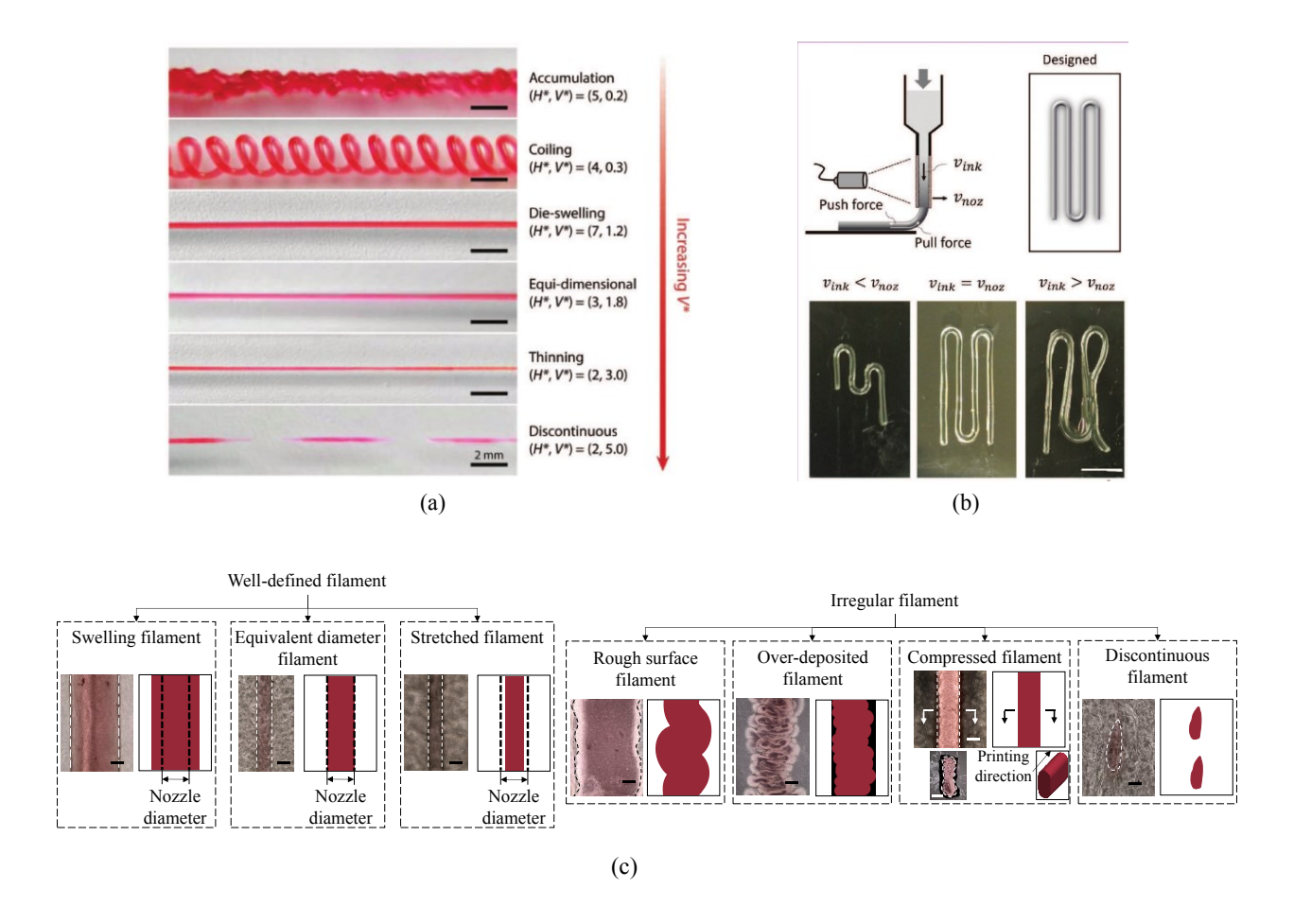


Figure 13. (a) Different types of filaments¹⁸⁰ and (b) printing fidelity investigations¹⁸³ during self-supporting rapid solidification printing, and (c) different types of filaments during support bath-enabled printing.¹⁰³ Figures and captions are reproduced with permission from (1) Advanced Materials, **30**, 1704028 (2018). Copyright 2017 WILEY-VCH Verlag GmbH & Co. KGaA, Weinheim, (2) Advanced Materials, **29**, 1604983 (2017). Copyright 2016 WILEY-VCH Verlag GmbH & Co. KGaA, Weinheim, and (3) Materials Science and Engineering C, **80**, 313 (2017). Copyright 2017 Elsevier B.V.

3.3.2 Micro-extrusion bioprinting phase diagram

During self-supporting rapid solidification, filaments are extruded through a nozzle in a liquid state. Thus, before depositing on a substrate and being cross-linked, the extruded filaments may break up into droplets at a standoff distance, which is similar to the pinch-off process during inkjet bioprinting. Figure 14a shows a phase diagram revealing the relationship between the gelation condition of printed filaments and the ratio $\Delta t_{gel}/\Delta t_{layer}$, where Δt_{layer} is the time for printing between two layers and Δt_{gel} is the gelation time.

During support bath-enabled printing, the supporting bath material yields and is displaced around the nozzle as it translates through the bath. The yielded dimensions of a given support bath around a translating nozzle need to be optimized for better printability of bioinks. Different phase diagrams have been proposed to rationalize such a process. In particular, the Oldroyd number (Od as seen from Table 1) was used to characterize the dimensions of the yielded areas of a Herschel-Bulkley fluid flowing around a cylinder. 101 It is found that Od has significant effects on the dimensionless yielded width (W/d) that is defined as the ratio of the entire width (W) of the yielded region and the nozzle outer diameter (d). The higher Od leads to smaller dimensionless yielded regions around the nozzle. When Od < 1, the dimensionless width changes rapidly with changes in the Od, while when Od > 1, the dimensionless width changes less with changes in the Od. In addition, the print fidelity increases with the increasing Od when a print path is selected that minimizes the exposure of previously patterned features to support bath yielding around the translating nozzle. 101 Jin et al. 103 constructed a phase diagram to guide the selection of support bath materials, bioinks and operating conditions. Using the aforementioned dimensionless ratios (speed ratio ($v = v_{path} / v_{out}$) and storage modulus ratio (G'_{bath}/G'_{ink})), a twodimensional phase diagram (Figure 14b) was proposed from which the formation of different types of filaments in the nanoclay support bath can be characterized. In addition, the conditions to form well-defined filaments with a controllable diameter can be predicted based on the phase diagram. Regardless of the type of support baths, their thixotropic behavior as well as the thixotropic time must be satisfied in order to allow the bath material to fill any crevice generated during printing.

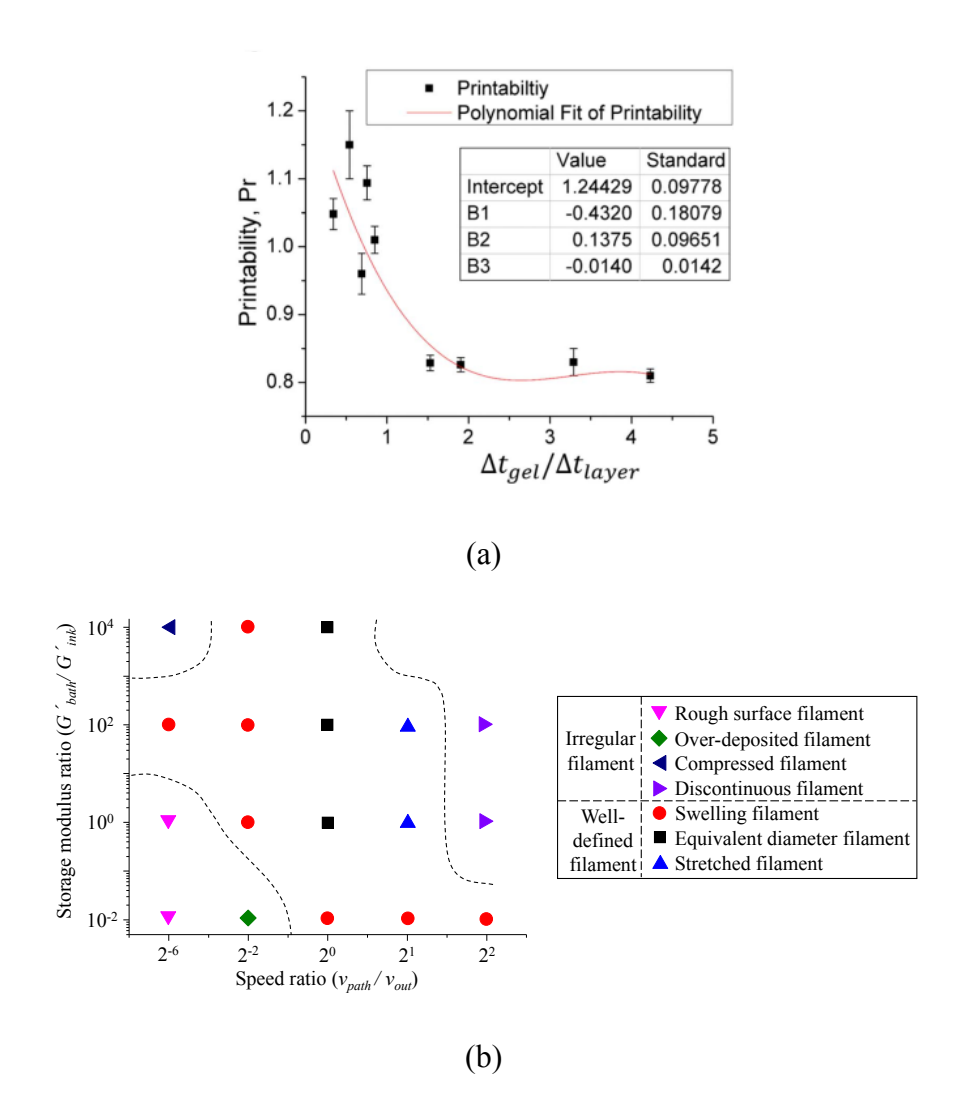


Figure 14. (a) Phase diagram to demonstrate the gelation condition of printed filaments during self-supporting rapid solidification-based micro-extrusion¹⁰² and (b) phase diagram during support bath-enabled printing.¹⁰³ Figures and captions are reproduced with permission from (1) Biofabrication, **8**, 035020 (2016). Copyright 2016 IOP Publishing Ltd. and (2) Materials Science and Engineering C, **80**, 313 (2017). Copyright 2017 Elsevier B.V.

3.4 Comparisons of bioprinting techniques, typical bioink compositions and cell viability

In addition to the bioink printability review, each printing technique/modality has also been compared in terms of their typical hydrogels, cell types and their concentrations, and the post-printing cell viability. The information, illustrated in Table 3, provides further information about the suitable cell-laden bioinks for each bioprinting technique as well as their appropriate applications. It noted that the effects of printing parameters on the post-printing cell viability have also been investigated for inkjet printing, laser printing, and micro-extrusion, respectively. For example, Zhang *et al.* 117 investigated the effects of excitation voltage on the post-printing viability during inkjet printing. It is observed that the cell viability decreases as the excitation voltage increases. Gudapati *et al.* 191 studied the effects of laser fluence on the post-printing cell viability during laser printing of 3T3 fibroblast-laden alginate/DMEM bioinks. The results indicate that the post-printing viability decreases as the laser fluence increases. During extrusion printing HepG2 cell-laden alginate bioinks, Chang *et al.* 30 showed that the cell viability decreases as the dispensing pressure increases or the nozzle size decreases.

Table 3. Comparisons of bioprinting techniques, typical bioink compositions and cell viability

Bioprinting technique	Hydrogel	Cell types and their concentration	Cell viability
Inkjet printing	Alginate	NIH 3T3 mouse fibroblasts (1×10^6 cells/mL), 192 NIH 3T3 mouse fibroblasts (5×10^6 cells/mL), 21 and HeLa cells (6×10^6 cells/mL) 108	70%~95%
	Collagen type I	Bladder smooth muscle cells (0.1-1×10 ⁶ cells/mL), ¹⁹³ Rabbit articular chondrocytes (3-4×10 ⁶ cells/mL), ¹⁹⁴ Bladder smooth muscle cells (1-10×10 ⁶ cells/mL), ¹⁹⁵ Amniotic fluid-derived stem cells (1.66×10 ⁷ cells/mL), ¹⁹⁶ and Bone marrow-derived mesenchymal stem cells (1.66×10 ⁷ cells/mL) ¹⁹⁶	80%~>90%
	Fibrin	Human microvascular endothelial cells (1-8×10 ⁶ cells/mL) ¹²³	Not available
	Methacrylated gelatin (GelMA)	Human mesenchymal stem cells (1×10 ⁶ cells/mL) ¹⁹⁷	>90%
	Polyethylene glycol (PEG)	Human articular cartilage (5×10 ⁶ cells/mL), ²⁵ Bone marrow-derived human mesenchymal stem cells (6×10 ⁶ cells/mL), ¹⁹⁸ and Human articular cartilage (8×10 ⁶ cells/mL) ¹⁹⁹	80%~89%
Laser printing	Alginate	NIH 3T3 mouse fibroblasts $(5\times10^6 \text{ cells/mL})$, 19,191 B16 carcinoma cell $(4\times10^7 \text{ cells/mL})$, 200 Adipose-derived human mesenchymal stem cells $(1-2\times10^6 \text{ cells in } 30 \text{ µL})$, 201 Bone marrow-derived human mesenchymal stem cells $(1-2\times10^6 \text{ cells in } 30 \text{ µL bioink})$, 201 HaCaT keratinocytes $(1-2\times10^6 \text{ cells in } 30 \text{ µL bioink})$, 201 and NIH 3T3 mouse fibroblasts $(1-2\times10^6 \text{ cells in } 30 \text{ µL bioink})$ cells in 30 µL bioink).	72%~98%
	Collagen type I	HaCaT keratinocytes (1.5×10 ⁶ cells resuspended in 1×DMEM/Ham's F12 medium (22.5% of the total volume)) ²⁰² and NIH 3T3 mouse fibroblasts (1.5×10 ⁶ cells resuspended in 1×DMEM/Ham's F12 medium (22.5% of the total volume)) ²⁰²	Not available
	Fibrin	B16 carcinoma cell $(0.5-1\times10^8 \text{ cells/mL})^{200}$ and Eahy926 endothelial cell $(0.5-1\times10^8 \text{ cells/mL})^{200}$	Not available
	Matrigel	Pluripotent murine embryonal carcinoma cells (1.5×10 ⁷ cells/mL) ¹²⁹ and Eahy926 endothelial cell (6×10 ⁷ cells/mL) ²⁰⁰	>95%
	Gelatin	Human dermal fibroblast cells (1×10^6) cells on the ribbon made from 1.5 mL gelatin $(20\%)^{203}$	91±3% (Day 1)
Micro- extrusion	Agarose	Bone marrow stromal cells (2.5×10 ⁵ cells/mL), ²⁰⁴ Human mesenchymal stromal cells (1-1.6×10 ⁶ cells/mL), ¹⁷³ Bone marrow-derived human mesenchymal stem cells (1×10 ⁷ cells/mL), ²⁰⁵ and MG-63 osteosarcoma-derived cells (1×10 ⁷ cells/mL) ²⁰⁵	90%-~100%
	Alginate	Bone marrow stromal cells (2.5×10 ⁵ cells/mL), ²⁰⁴ Human adipose derived stem cells (1×10 ⁶ cells/mL), ²⁰⁶ Aortic root sinus smooth muscle cells (2×10 ⁶ cells/mL), ¹⁶⁶ Aortic valve leaflet interstitial cells (2×10 ⁶ cells/mL), ¹⁶⁶ Cartilage progenitor cells (2×10 ⁶ cells/mL), ²⁰⁷ Goat multipotent stromal cells (1×10 ⁷ cells/mL), ²⁰⁸ Human articular chondrocytes (0.3-1×10 ⁷ cells/mL), ²⁰⁹ Bone marrow-derived human mesenchymal stem cells (0.5-1×10 ⁷ cells/mL), ²⁰⁹ and Human cardiac-derived cardiomyocyte progenitor cells (3×10 ⁷ cells/mL) ²¹⁰	62.7%-~95%

	Chitosan	Human mesenchymal stromal cells (1-1.6×10 ⁶ cells/mL) ¹⁷³	~100%
	Collagen type I	Human mesenchymal stromal cells (1-1.6×10 ⁶ cells/mL) ¹⁷³ and Bovine aortic endothelial	~86%~100%
		cells (5-20×10 ⁶ cells/mL) ²¹¹	
	Fibrin	Hepatic cells $(1 \times 10^6 \text{ cells/mL})^{212}$	~98%
	Gelatin	Rat hepatocytes $(1 \times 10^6 \text{ cells/mL})$, ²¹³ Aortic root sinus smooth muscle cells $(2 \times 10^6 \text{ m})$	81.4 %~ 83.2 %
		cells/mL), 166 and Aortic valve leaflet interstitial cells (2×106 cells/mL) 166	
	Methacrylated gelatin (GelMA)	HepG2 human liver cancer cells $(1.5\times10^6 \text{ cells/mL})$, ¹⁷⁷ HepG2 human liver cancer cells $(1-6\times10^6 \text{ cells/mL})$, ¹⁶⁹ and NIH 3T3 mouse fibroblasts $(1-6\times10^6 \text{ cells/mL})$, ¹⁶⁹	~90%->97%
	Hyaluronic acid	HepG2 C3A human liver cancer cells (2.5×10 ⁷ cells/mL) ²¹⁴	Not available
-	Matrigel Matrigel	Bone marrow stromal cells $(2.5 \times 10^5 \text{ cells/mL})$, ²⁰⁴ HepG2 human liver cancer cells $(1.0 \times 10^6 \text{ m})$	~95%
	Maurger	cells/mL), ²¹⁵ M10 human mammary epithelial (1.0×10 ⁶ cells/mL), ²¹⁵ Bone marrow-derived	~93%
		cens/mL), M10 numan mammary epinenai (1.0×10 cens/mL), Bone marrow-derived	
		goat mesenchymal stem cells $(5\times10^6 \text{ cells/mL})^{216}$ and Peripheral blood-derived goat endothelial progenitor cells $(5\times10^6 \text{ cells/mL})^{216}$	
	Methylcellulose	Bone marrow stromal cells $(2.5 \times 10^5 \text{ cells/ml})^{204}$ and Human nasoseptal chondrocytes $(1.5 \times 10^7 \text{ cells/ml})^{174}$	73%~86%
	Polyethylene	Bone marrow-derived human mesenchymal stem cells (3×10 ⁶ cells/ml) ²¹⁷	86%
	glycol (PEG)	•	
	Pluronic® F-127	Bone marrow stromal cells $(2.5 \times 10^5 \text{ cells/ml})^{204}$ and Human primary fibroblasts (no	~60%-~85%
		concentration information) ²¹¹	

4. Conclusions and Future Work

Three-dimensional (3D) bioprinting has emerged as a promising solution to some of the obstacles facing by the tissue engineering, including vascularization of thick tissue constructs, precise placement of multiple cell types, and achieving organ-specific level of cell density in tissue constructs. In general, 3D printing is the positioning of build materials in a layer-by-layer fashion. During 3D bioprinting, materials printed are usually refereed as bioinks, which may include living cells (either suspended or as cell aggregates), extracellular matrix materials such as applicable hydrogels, cell media, and/or other additives. However, the lack of suitable bioinks with good printability has been one of the most significant obstacles for scalable robotic bioprinting.

This review for the first time presents a comprehensive summary of the recent advances of bioink printability studies for the three most adopted bioprinting approaches: inkjet printing, laser printing, and micro-extrusion. In this study, the printability during inkjet bioprinting is characterized based on its ability to generate well-defined single droplets in air. The printability of bioink during laser printing is defined as the ability to generate well-defined jets during the jet and droplet formation process as well as well-defined printed droplets on a receiving substrate during the jet and droplet deposition process. In extrusion-based bioprinting, the printability is defined as the capability of bioinks to form continuous filaments with a controllable diameter and well-defined morphology, which is considered the extrudability, and further form well-defined 3D structures, which is considered the formability. Generally, once a well-defined droplet or filament can be formed, it is feasible to produce 3D structures/constructs with good fidelity and integrity.

Different jetting/printing regimes have been identified under different combinations of bioink material properties and operating/printing conditions. In particular, phase diagrams have been constructed based on different groups of dimensionless numbers to effectively summarize the knowledge of various bioink printability studies. Some notable conclusions are listed as follows:

- For inkjet printing, the Z number (the inverse of Ohnesorge number), Weber number, and capillary number have been employed for the construction of phase diagrams during the printing of Newtonian fluids while the Weissenberg and Deborah numbers have been utilized during the printing of non-Newtonian bioinks.
- Four breakup types, namely front pinching, hybrid pinching, exit pinching, and middle pinching, have been identified based on the first pinch-off location during inkjet printing of viscoelastic alginate solutions. If living cells are added into bioinks, the inks become soft particle-laden suspensions. When the cell concentration of a bioink increases, the droplet size and velocity decrease, the formation of satellite droplets is suppressed, and the breakup time increases. When compared to a hard bead (polystyrene)-laden suspension, cell-laden bioink has a smaller ejected fluid volume, lower droplet velocity, and longer breakup time.
- During the laser printing of Newtonian solutions, the jettability can be characterized as the inverse of the Ohnesorge number. During the laser printing of viscoelastic alginate solutions, five jetting regimes have been identified: no material transfer, well-defined jetting, well-defined jetting with an initial bulgy shape, jetting with a bulgy shape, and pluming/splashing.
- For laser printing, Ohnesorge, elasto-capillary, and Weber numbers have been utilized to construct phase diagrams to study the dependence of jetting regimes on the laser fluence and concentration of typical non-Newtonian bioinks. Weber number-defined planes can be used

- to distinguish different jetting regimes. The increase of viscous and elastic effects helps stabilize the jetting process or even suppress the formation of jets.
- The printability of cell-laden bioinks can be mapped in the same two Weber-Ohnesorge and Weber-elasto-capillary phase diagrams as during the laser printing of non-Newtonian fluids. The effects of cell media and living cells on the bioink printability can be sufficiently captured by the material property-related Ohnesorge and elasto-capillary numbers.
- Non-ideal jetting behaviors are common during droplet-based inkjet and laser printing processes due to the local nonuniformity and nonhomogeneity of cell-laden bioinks.
- For micro-extrusion, seven filament types have been identified during support bath-enabled extrusion including three types of well-defined filaments (swelling filament, equivalent diameter filament, and stretched filament) and four types of irregular filaments (rough surface filament, over-deposited filament, compressed filament, and discontinuous filament) based on material properties and operating conditions.
- During micro-extrusion, the Oldroyd number has been used to characterize the dimensions of the yielded areas of Herschel-Bulkley fluids flowing around a cylinder. In addition, dimensionless ratios (speed ratio and storage modulus ratio) have been used to construct a two-dimensional phase diagram to distinguish the formation of different types of filaments.
- Since the micro-extrusion process is a slowly dispensing process, jetting is usually avoided and non-ideal jetting behaviors are not of interest. The deposited cellular filaments and extrusion printability are not specifically investigated since the local nonuniformity and nonhomogeneity of living cells don't significantly alter the macroscopic material properties of cell-laden bioinks.

Important areas of future work should include: 1) revealing the underlying physics of the breakup of fluid jets during droplet-based printing and filaments during filament-based printing by investing the formation process of viscoelastic solutions as well as cell-laden viscoelastic suspensions, 2) developing mathematical analysis of the filament formation mechanism during support bath-enabled micro-extrusion, in particular, a model to include the elastic effects of printed bioinks, and 3) constructing unified phase diagrams for bioink printability evaluation based on material properties and operating conditions.

Acknowledgements

This study was partially supported by the National Natural Science Foundation of China (51709120) (Z.Z.) and U.S. National Science Foundation (1537956, 1634755, and 1762941) (Y.H.). The leadership by Dr. Anthony Atala and Prof. Roger Narayan on this bioprinting topic is highly appreciated.

References

- 1. R. Langer and J. P. Vacanti, Science **260**, 920 (1993).
- 2. D. E. Ingber, V. C. Mow, D. L. Butler, L. E. Niklason, J. Huard, J. J. Mao, I. V. Yannas, D. L. Kaplan, and G. Vunjaknovakovic, Tissue Engineering 12, 3265 (2006).
- 3. R. Lanza; R. Langer, and J. Vacanti, Academic Press, (2014).
- 4. Y. Huang and S. R. Schmid, Journal of Manufacturing Science and Engineering, **140**, 094001 (2018).
- 5. D. W. Hutmacher, Biomaterials **21**, 2529 (2000).
- 6. S. J. Hollister, Nature Materials 4, 518 (2005).

- K. E. Kasza, A. C. Rowat, J. Liu, T. E. Angelini, C. P. Brangwynne, G. H. Koenderink, and D.
 A. Weitz, Current Opinion in Cell Biology 19, 101 (2007).
- 8. B. Derby, Science **338**, 921 (2012).
- 9. L. E. Freed, G. Vunjak-Novakovic, R. J. Biron, D. B. Eagles, D. C. Lesnoy, S. K. Barlow, and R. Langer, Nature Biotechnology **12**, 689 (1994).
- 10. S. V. Madihally and H. W. T. Matthew, Biomaterials 20, 1133 (1999).
- 11. S. Yang, K. F. Leong, Z. H. Du, and C. K. Chua, Tissue Engineering 7, 679 (2001).
- 12. J. M. Kelm and M. Fussenegger, Trends in Biotechnology 22, 195 (2004).
- 13. J. Yang, M. Yamato, C. Kohno, A. Nishimoto, H. Sekine, F. Fukai, and T. Okano, Biomaterials **26**, 6415 (2005).
- 14. J. M. Kelm, V. Djonov, L. M. Ittner, D. A. Fluri, W. Born, S. P. Hoerstrup, and M. Fussenegger, Tissue Engineering **12**, 2151 (2006).
- 15. J. W. Nichol and A. Khademhosseini, Soft Matter 5, 1312 (2009).
- 16. A. Khademhosseini, R. Langer, J. T. Borenstein, and J. P. Vacanti, Proceedings of the National Academy of Sciences of the United States of America **103**, 2480 (2006).
- 17. R. Langer, Tissue Engineering **13,** 1 (2007).
- 18. V. Mironov, R. P. Visconti, V. Kasyanov, G. Forgacs, C. J. Drake, and R. R. Markwald, Biomaterials **30**, 2164 (2009).
- Z. Zhang, W. Chai, R. Xiong, L. Zhou, and Y. Huang, Biofabrication 9, 025038 (2017).DOI: 10.1088/1758-5090/aa6ed9/
- 20. H. Yong, C. L. Ming, J. Mazumder, and A. Donmez, Journal of Manufacturing Science & Engineering 137, 014001 (2015).

- 21. K. Christensen, C. Xu, W. Chai, Z. Zhang, J. Fu, and Y. Huang, Biotechnology and bioengineering **112**, 1047 (2015).
- 22. R. Xiong, Z. Zhang, W. Chai, Y. Huang, and D. B. Chrisey, Biofabrication 7, 045011 (2015).
- M. S. Mannoor, Z. Jiang, T. James, Y. L. Kong, K. Malatesta, W. O. Soboyejo, N. Verma, D. H. Gracias, and M. C. Mcalpine, Nano Letters 13, 2634 (2013).
- 24. C. Xu, W. Chai, Y. Huang, and R. R. Markwald, Biotechnology and Bioengineering 109, 3152 (2012).
- 25. X. Cui, K. Breitenkamp, M. Finn, M. Lotz, and D. D. D'Lima, Tissue Engineering Part A 18, 1304 (2012).
- 26. M. K. Gupta, F. Meng, B. N. Johnson, Y. L. Kong, L. Tian, Y. W. Yeh, N. Masters, S. Singamaneni, and M. C. Mcalpine, Nano Letters **15**, 5321 (2015).
- 27. L. Setti, A. Fraleonimorgera, B. Ballarin, A. Filippini, D. Frascaro, and C. Piana, Biosensors and Bioelectronics **20**, 2019 (2005).
- 28. M. D. Symes, P. J. Kitson, J. Yan, C. J. Richmond, G. J. T. Cooper, R. Bowman, T. Vilbrandt, and L. Cronin, Nature Chemistry 4, 349 (2012).
- 29. D. Falconnet, G. Csucs, H. M. Grandin, and M. Textor, Biomaterials 27, 3044 (2006).
- 30. R. Chang, J. Nam, and W. Sun, Tissue Engineering Part C: Methods 14, 157 (2008).
- 31. M. Matsusaki, K. Sakaue, K. Kadowaki, and M. Akashi, Advanced Healthcare Materials **2**, 534 (2013).
- 32. C. Fischbach, R. Chen, T. Matsumoto, T. Schmelzle, J. S. Brugge, P. J. Polverini, and D. J. Mooney, Nature methods **4**, 855 (2007).
- 33. J. Jang, H. Yi, and D. Cho, ACS Biomaterials Science & Engineering 2, 1722 (2016).
- 34. S. V. Murphy and A. Atala, Nature Biotechnology **32**, 773 (2014).

- 35. J. L. West and J. A. Hubbell, Macromolecules **32**, 241 (1999).
- 36. D. Chimene, K. K. Lennox, R. R. Kaunas, and A. K. Gaharwar, Annals of biomedical engineering 44, 2090 (2016).
- 37. J. Malda, J. Visser, F. P. W. Melchels, T. Jungst, W. E. Hennink, W. J. A. Dhert, J. Groll, and D. W. Hutmacher, Advanced Materials **25**, 5011 (2013).
- 38. T. Jungst, W. Smolan, K. Schacht, T. Scheibel, and J. Groll, Chemical Reviews **116**, 1496 (2016).
- 39. M. M. Stanton, J. Samitier, and S. Sanchez, Lab on a Chip 15, 3111 (2015).
- 40. R. R. Jose, M. J. Rodriguez, T. A. Dixon, F. G. Omenetto, and D. L. Kaplan, ACS Biomaterials Science & Engineering 2, 1662 (2016).
- 41. A. M. Compaan, K. Christensen, and Y. Huang, ACS Biomaterials Science & Engineering **3**, 1519 (2016).
- 42. H. C. Ott, T. S. Matthiesen, S. K. Goh, L. D. Black, S. M. Kren, T. I. Netoff, and D. A. Taylor, Nature Medicine **14**, 213 (2008).
- 43. F. Pati, J. Jang, D. H. Ha, S. W. Kim, J. W. Rhie, J. H. Shim, D. H. Kim, and D. W. Cho, Nature Communications 5, 3935 (2014).
- 44. J. Malda and C. G. Frondoza, Trends in Biotechnology 24, 299 (2006).
- 45. R. Levato, J. Visser, J. A. Planell, E. Engel, J. Malda, and M. A. Mateostimoneda, Biofabrication **6**, 035020 (2014).
- 46. K. Jakab, F. Marga, C. Norotte, K. Murphy, G. Vunjak-Novakovic, and G. Forgacs, Biofabrication **2**, 022001 (2010).
- 47. C. Norotte, F. S. Marga, L. E. Niklason, and G. Forgacs, Biomaterials 30, 5910 (2009).
- 48. C. Owens, F. Marga, G. Forgacs, and C. M. Heesch, Biofabrication 5, 045007 (2013).

- 49. J. H. Chung, S. Naficy, Z. Yue, R. Kapsa, A. Quigley, S. E. Moulton, and G. G. Wallace, Biomaterials Science 1, 763 (2013).
- 50. Y. Jin, A. M. Compaan, T. Bhattacharjee, and Y. Huang, Biofabrication 8, 025016 (2016).
- 51. Q. Chen, H. Chen, L. Zhu, and J. Zheng, Journal of Materials Chemistry B 3, 3654 (2015).
- 52. S. E. Bakarich, R. Gorkin, M. I. H. Panhuis, and G. M. Spinks, Macromolecular rapid communications **36**, 1211 (2015).
- 53. A. K. Gaharwar, N. A. Peppas, and A. Khademhosseini, Biotechnology & Bioengineering 111, 441 (2014).
- 54. T. Ahlfeld, G. Cidonio, D. Kilian, S. Duin, A. Akkineni, J. Dawson, S. Yang, A. Lode, R. Oreffo, and M. Gelinsky, Biofabrication **9**, 034103 (2017).
- 55. C. B. Highley, C. B. Rodell, and J. A. Burdick, Advanced Materials 27, 5075 (2015).
- 56. M. Kesti, M. Muller, J. Becher, M. Schnabelrauch, M. D. Este, D. Eglin, and M. Zenobiwong, Acta Biomaterialia 11, 162 (2015).
- 57. J. A. Rowley, G. Madlambayan, and D. J. Mooney, Biomaterials 20, 45 (1999).
- 58. E. M. Ahmed, Journal of advanced research 6, 105 (2015).
- 59. M. Hospodiuk, M. Dey, D. Sosnoski, and I. T. Ozbolat, Biotechnology Advances **35**, 217 (2017).
- 60. J. L. Drury and D. J. Mooney, Biomaterials 24, 4337 (2003).
- 61. B. C. Riggs, A. D. Dias, N. R. Schiele, R. Cristescu, Y. Huang, D. T. Corr, and D. B. Chrisey, Mrs Bulletin **36**, 1043 (2011).
- 62. V. Chan, J. H. Jeong, P. Bajaj, M. Collens, T. Saif, H. Kong, and R. Bashir, Lab on a Chip 12, 88 (2012).

- 63. X. Ma, X. Qu, W. Zhu, Y. Li, S. Yuan, H. Zhang, J. Liu, P. Wang, C. S. E. Lai, and F. Zanella, Proceedings of the National Academy of Sciences of the United States of America 113, 2206 (2016).
- 64. M. S. Jhon and J. D. Andrade, Journal of Biomedical Materials Research 7, 509 (1973).
- 65. M. W. Tibbitt and K. S. Anseth, Biotechnology and Bioengineering 103, 655 (2009).
- 66. B. Thomas, J. C. Fryman, K. Liu, and J. J. Mason, Journal of the Mechanical Behavior of Biomedical Materials **2**, 588 (2009).
- 67. J. Zhu and R. E. Marchant, Expert Review of Medical Devices 8, 607 (2011).
- 68. K. Y. Lee and D. J. Mooney, Chemical Reviews **101**, 1869 (2001).
- 69. Q. Ye, G. Zünd, P. Benedikt, S. Jockenhoevel, S. P. Hoerstrup, S. Sakyama, J. A. Hubbell, and M. Turina, European Journal of Cardio-Thoracic Surgery 17, 587 (2000).
- 70. N. Rajan, J. Habermehl, M. F. Coté, C. J. Doillon, and D. Mantovani, Nature Protocols 1, 2753 (2006).
- 71. M. Yamamoto, D. James, H. Li, J. M. Butler, S. Rafii, and S. Y. Rabbany, Tissue Engineering Part A 16, 299 (2010).
- 72. K. Ye, R. Felimban, K. Traianedes, S. E. Moulton, G. G. Wallace, J. Chung, A. Quigley, P. F. Choong, and D. E. Myers, Plos One **9**, e99410 (2014).
- 73. F. Croisier and C. Jérôme, European Polymer Journal 49, 780 (2013).
- 74. L. Pescosolido, W. Schuurman, J. Malda, P. Matricardi, F. Alhaique, T. Coviello, P. R. Van Weeren, W. J. A. Dhert, W. E. Hennink, and T. Vermonden, Biomacromolecules **12**, 1831 (2011).
- 75. J. A. Burdick and G. D. Prestwich, Advanced materials 23, H41 (2011).
- 76. K. Y. Lee and D. J. Mooney, Progress in Polymer Science 37, 106 (2012).

- 77. L. Gasperini, J. F. Mano, and L. R. Rui, Journal of the Royal Society Interface **11**, 20140817 (2014).
- 78. M. D. Biase, R. E. Saunders, N. Tirelli, and B. Derby, Soft Matter 7, 2639 (2011).
- 79. B. Derby, Journal of Materials Chemistry 18, 5717 (2008).
- 80. N. R. Schiele, D. T. Corr, Y. Huang, N. A. Raof, Y. Xie, and D. B. Chrisey, Biofabrication 2, 032001 (2010).
- 81. C. C. Chang, E. D. Boland, S. K. Williams, and J. B. Hoying, Journal of Biomedical Materials Research Part B: Applied Biomaterials **98**, 160 (2011).
- 82. B. R. Ringeisen, R. K. Pirlo, P. K. Wu, T. Boland, Y. Huang, W. Sun, Q. Hamid, and D. B. Chrisey, Mrs Bulletin **38**, 834 (2013).
- 83. I. T. Ozbolat and Y. Yu, IEEE Transactions on Biomedical Engineering 60, 691 (2013).
- 84. I. T. Ozbolat and M. Hospodiuk, Biomaterials 76, 321 (2016).
- 85. H. Gudapati, M. Dey, and I. Ozbolat, Biomaterials 102, 20 (2016).
- 86. N. E. Fedorovich, J. Alblas, J. R. de Wijn, W. E. Hennink, A. J. Verbout, and W. J. Dhert, Tissue engineering **13**, 1905 (2007).
- 87. S. V. Murphy, A. Skardal, and A. Atala, Journal of Biomedical Materials Research Part A **101**, 272 (2013).
- 88. F. P. W. Melchels, M. Domingos, T. J. Klein, J. Malda, P. J. Bartolo, and D. W. Hutmacher, Progress in Polymer Science **37**, 1079 (2012).
- 89. I. T. Ozbolat, Trends in Biotechnology **33**, 395 (2015).
- 90. K. Kim, W. Zhu, X. Qu, C. Aaronson, W. R. Mccall, S. Chen, and D. J. Sirbuly, Acs Nano 8, 9799 (2014).

- 91. X. Ma, X. Qu, W. Zhu, Y. S. Li, S. Yuan, H. Zhang, J. Liu, P. Wang, C. S. Lai, F. Zanella G. Feng, F. Sheikh, S. Chien, and S. Chen, Proceedings of the National Academy of Sciences of the United States of America 113, 2206 (2016).
- 92. X. Ma, C. Yu, P. Wang, W. Xu, X. Wan, C. S. E. Lai, J. Liu, A. Koroleva-Maharajh, and S. Chen, Biomaterials **185**, 310 (2018).
- 93. N. C. Paxton, W. Smolan, T. Böck, F. Melchels, J. Groll, and T. Juengst, Biofabrication 9, 044107 (2017).
- 94. C. Clasen, P. M. Phillips, L. Palangetic, and A. J. Vermant, AIChE Journal 58, 3242 (2012).
- 95. E. Kim and J. Baek, Physics of Fluids 24, 082103 (2012).
- 96. S. D. Hoath, O. G. Harlen, and I. M. Hutchings, Journal of Rheology 56, 1109 (2012).
- 97. G. H. Mckinley and M. Renardy, Physics of Fluids 23, 127101 (2011).
- 98. J. Fromm, IBM Journal of Research and Development 28, 322 (1984).
- 99. D. Jang, D. Kim, and J. Moon, Langmuir **25**, 2629 (2009).
- 100. J. Yan, Y. Huang, C. Xu, and D. B. Chrisey, Journal of Applied Physics 112, 083105 (2012).
- 101. A. K. Grosskopf, R. L. Truby, H. Kim, A. Perazzo, J. A. Lewis, and H. A. Stone, ACS Applied Materials & Interfaces 10, 23353 (2018).
- 102. L. Ouyang, R. Yao, Y. Zhao, and W. Sun, Biofabrication 8, 035020 (2016).
- 103. Y. Jin, W. Chai, and Y. Huang, Materials Science and Engineering: C 80, 313 (2017).
- 104. C. L. Herran, W. Wang, Y. Huang, V. Mironov, and R. Markwald, Journal of Manufacturing Science & Engineering 132, 635 (2010).
- 105. T. Xu, J. Jin, C. Gregory, J. J. Hickman, and T. Boland, Biomaterials 26, 93 (2005).

- 106. M. Nakamura, A. Kobayashi, F. Takagi, A. Watanabe, Y. Hiruma, K. Ohuchi, Y. Iwasaki, M. Horie, I. Morita, and S. Takatani, Tissue Engineering 11, 1658 (2005).
- 107. T. Xu, C. Gregory, P. Molnar, X. Cui, S. Jalota, S. B. Bhaduri, and T. Boland, Biomaterials **27,** 3580 (2006).
- 108. Y. Nishiyama, M. Nakamura, C. Henmi, K. Yamaguchi, S. Mochizuki, H. Nakagawa, and K. Takiura, Journal of Biomechanical Engineering-transactions of The Asme **131**, 035001 (2009).
- 109. R. Saunders, J. E. Gough, and B. Derby, Biomaterials **29**, 193 (2008).
- 110. J. D. Kim, J. S. Choi, B. S. Kim, Y. C. Choi, and Y. W. Cho, Polymer **51**, 2147 (2010).
- 111. P. Calvert, Science 318, 208 (2007).
- 112. C. Xu, Journal of Manufacturing Science & Engineering 136, 061020 (2014).
- 113. H. Dong, W. W. Carr, and J. F. Morris, Physics of fluids 18, 072102 (2006).
- 114. X. Yan, W. W. Carr, and H. Dong, Physics of Fluids 23, 107101 (2011).
- 115. C. Xu, Z. Zhang, J. Fu, and Y. Huang, Langmuir **33**, 5037 (2017).
- 116. C. Xu, M. Zhang, Y. Huang, A. Ogale, J. Fu, and R. R. Markwald, Langmuir **30,** 9130 (2014).
- 117. M. Zhang, S. Krishnamoorthy, H. Song, Z. Zhang, and C. Xu, Journal of Applied Physics 121, 124904 (2017).
- 118. Y. Lin, Y. Huang, and D. B. Chrisey, Journal of Applied Physics 105, 093111 (2009).
- 119. A. Piqué, D. B. Chrisey, R. C. Y. Auyeung, J. Fitz-Gerald, H. D. Wu, R. A. Mcgill, S. Lakeou, P. K. Wu, V. Nguyen, and M. Duignan, Applied Physics A 69, S279 (1999).
- 120. R. Xiong, Z. Zhang, J. Shen, Y. Lin, Y. Huang, and D. B. Chrisey, Journal of Micro and Nano-Manufacturing **3**, 011004 (2015).

- 121. Z. Zhang, R. Xiong, R. Mei, Y. Huang, and D. B. Chrisey, Langmuir 31, 6447 (2015).
- 122. Z. Zhang, R. Xiong, D. T. Corr, and Y. Huang, Langmuir 32, 3004 (2016).
- 123. X. Cui and T. Boland, Biomaterials **30**, 6221 (2009).
- 124. J. Yan, Y. Huang, and D. B. Chrisey, Biofabrication 5, 015002 (2013).
- 125. V. Dinca, E. Kasotakis, J. Catherine, A. Mourka, A. Ranella, A. Ovsianikov, B. N. Chichkov, M. Farsari, A. Mitraki, and C. Fotakis, Nano Letters **8,** 538 (2008).
- 126. M. Colina, P. Serra, J. M. Fernández-Pradas, L. Sevilla, and J. L. Morenza, 20, 1638 (2005).
- 127. D. B. Chrisey, Science **289**, 879 (2000).
- 128. J. Barron, P. Wu, H. Ladouceur, and B. Ringeisen, Biomedical microdevices 6, 139 (2004).
- 129. B. R. Ringeisen, H. Kim, J. A. Barron, D. B. Krizman, D. B. Chrisey, S. Jackman, R. Y. C. Auyeung, and B. J. Spargo, Tissue Engineering **10**, 483 (2004).
- 130. Y. Lin, Y. Huang, G. Wang, T. J. Tzeng, and D. B. Chrisey, Journal of Applied Physics **106**, 043106 (2009).
- 131. F. Guillemot, A. Souquet, S. Catros, B. Guillotin, J. Lopez, M. Faucon, B. Pippenger, R. Bareille, M. Rémy, and S. Bellance, Acta Biomaterialia **6**, 2494 (2010).
- 132. M. Gruene, M. Pflaum, C. Hess, S. Diamantouros, S. Schlie, A. Deiwick, L. Koch, M. Wilhelmi, S. Jockenhoevel, and A. Haverich, Tissue Engineering Part C Methods 17, 973 (2011).
- Z. Zhang, C. Xu, R. Xiong, D. B. Chrisey, and Y. Huang, Biomicrofluidics 11, 034120 (2017). DOI:10.1063/1.4985652
- 134. M. Duocastella, J. Fernández-Pradas, J. Morenza, and P. Serra, Thin Solid Films **518**, 5321 (2010).
- 135. M. Duocastella, H. Kim, P. Serra, and A. Piqué, Applied Physics A 106, 471 (2012).

- 136. D. M. Kingsley, A. D. Dias, D. B. Chrisey, and D. T. Corr, Biofabrication 5, 045006 (2013).
- 137. M. Gruene, C. Unger, L. Koch, A. Deiwick, and B. Chichkov, Biomedical Engineering Online **10**, 19 (2011).
- 138. V. Dinca, M. Farsari, D. Kafetzopoulos, A. Popescu, M. Dinescu, and C. Fotakis, Thin Solid Films **516**, 6504 (2008).
- 139. M. Duocastella, M. Colina, J. Fernández-Pradas, P. Serra, and J. Morenza, Applied surface science **253**, 7855 (2007).
- 140. P. Serra, M. Duocastella, J. M. Fernández-Pradas, and J. L. Morenza, Applied Surface Science **255**, 5342 (2009).
- 141. M. Duocastella, J. M. Fernández-Pradas, J. Morenza, and P. Serra, Journal of applied physics **106**, 084907 (2009).
- 142. M. S. Brown, C. F. Brasz, Y. Ventikos, and C. B. Arnold, Journal of Fluid Mechanics **709**, 341 (2012).
- 143. C. Unger, M. Gruene, L. Koch, J. D. Koch, and B. N. Chichkov, Applied Physics A 103, 271 (2011).
- 144. B. Derby and N. Reis, MRS Bulletin 28, 815 (2003).
- 145. B. Ambravaneswaran, H. J. Subramani, S. D. Phillips, and O. A. Basaran, Physical review letters **93**, 034501 (2004).
- 146. H. J. Subramani, H. K. Yeoh, R. Suryo, Q. Xu, B. Ambravaneswaran, and O. A. Basaran, Physics of Fluids 18, 032106 (2006).
- 147. B. Derby, Annual Review of Materials Research 40, 395 (2010).

- 148. W. van Hoeve, S. Gekle, J. H. Snoeijer, M. Versluis, M. P. Brenner, and D. Lohse, Physics of Fluids **22**, 122003 (2010).
- 149. O. A. Basaran, H. Gao, and P. P. Bhat, Annual Review of Fluid Mechanics 45, 85 (2013).
- 150. P. P. Bhat, S. Appathurai, M. T. Harris, M. Pasquali, G. H. McKinley, and O. A. Basaran, Nature Physics **6**, 625 (2010).
- 151. N. F. Morrison and O. G. Harlen, Rheologica Acta 49, 619 (2010).
- 152. A. B. Dababneh and I. T. Ozbolat, Journal of Manufacturing Science and Engineering **136**, 061016 (2014).
- 153. F. Zhu, L. Cheng, J. Yin, Z. L. Wu, J. Qian, J. Fu, and Q. Zheng, ACS Applied Materials & Interfaces 8, 31304 (2016).
- 154. Y. Jin, A. M. Compaan, W. Chai, and Y. Huang, ACS Applied Materials & Interfaces 9, 20057 (2017).
- 155. Y. Jin, C. Liu, W. Chai, A. M. Compaan, and Y. Huang, ACS Applied Materials & Interfaces **9**, 17456 (2017).
- 156. J. Yin, M. Yan, Y. Wang, J. Fu, and H. Suo, ACS Applied Materials & Interfaces 10, 6849 (2018).
- 157. Y. Jin, Y. Shen, J. Yin, J. Qian, and Y. Huang, ACS Applied Materials & Interfaces 10, 10461 (2018).
- 158. J. Jang, H. Park, S. Kim, H. Kim, J. Y. Park, S. J. Na, H. J. Kim, M. N. Park, S. H. Choi, and S. H. Park, Biomaterials 112, 264 (2017).
- 159. F. Pati, D. Ha, J. Jang, H. H. Han, J. Rhie, and D. Cho, Biomaterials **62**, 164 (2015).

- 160. K. Jakab, C. Norotte, B. Damon, F. Marga, A. Neagu, C. Besch-Williford, A. Kachurin, K. Church, H. Park, V. Mironov, R. Markwald, G. Vunjak-Novakovic, and G. Forgacs, Tissue Engineering Part A 14, 413 (2008).
- 161. S. Vijayavenkataraman, W. F. Lu, and J. Y. Fuh, Biofabrication 8, 032001 (2016).
- 162. H. Shao, A. Liu, X. Ke, M. Sun, Y. He, X. Yang, J. Fu, L. Zhang, G. Yang, and Y. Liu, Journal of Materials Chemistry B 5, 2941 (2017).
- 163. A. C. Daly, S. E. Critchley, E. M. Rencsok, and D. J. Kelly, Biofabrication 8, 045002 (2016).
- 164. Z. Zhang, D. Jiang, J. Ding, S. Wang, L. Zhang, J. Zhang, Y. Qi, X. Chen, and J. Yu, Acta Biomaterialia 43, 314 (2016).
- 165. L. A. Hockaday, K. H. Kang, N. W. Colangelo, P. Y. Cheung, B. Duan, E. Malone, J. Wu, L. N. Girardi, L. J. Bonassar, and H. Lipson, Biofabrication 4, 035005 (2012).
- 166. B. Duan, L. A. Hockaday, K. H. Kang, and J. T. Butcher, Journal of biomedical materials research Part A **101**, 1255 (2013).
- 167. Y. Yu, Y. Zhang, J. A. Martin, and I. T. Ozbolat, Journal of Biomechanical Engineering-transactions of The ASME **135**, 091011 (2013).
- 168. B. N. Johnson, K. Z. Lancaster, G. Zhen, J. He, M. K. Gupta, Y. L. Kong, E. A. Engel, K. Krick, A. Ju, and F. Meng, Advanced Functional Materials **25**, 6205 (2015).
- 169. L. E. Bertassoni, J. C. Cardoso, V. Manoharan, A. L. Cristino, N. S. Bhise, W. A. Araujo, P. Zorlutuna, N. E. Vrana, A. M. Ghaemmaghami, M. R. Dokmeci, and A. Khademhosseini, Biofabrication 6, 024105 (2014).
- 170. B. Duan, E. Kapetanovic, L. A. Hockaday, and J. T. Butcher, Acta biomaterialia **10,** 1836 (2014).

- 171. J. Jia, D. Richards, S. Pollard, Y. Tan, J. Rodriguez, R. P. Visconti, T. C. Trusk, M. J. Yost, H. Yao, and R. R. Markwald, Acta Biomaterialia **10**, 4323 (2014).
- 172. S. Wust, M. E. Godla, R. Muller, and S. Hofmann, Acta Biomaterialia 10, 630 (2014).
- 173. D. F. Duarte Campos, A. Blaeser, A. Korsten, S. Neuss, J. Jäkel, M. Vogt, and H. Fischer, Tissue Engineering Part A **21**, 740 (2015).
- 174. K. Markstedt, A. Mantas, I. Tournier, H. M. Avila, D. Hagg, and P. Gatenholm, Biomacromolecules **16**, 1489 (2015).
- 175. A. G. Tabriz, M. A. Hermida, N. R. Leslie, and W. Shu, Biofabrication 7, 045012 (2015).
- 176. K. H. Kang, L. A. Hockaday, and J. T. Butcher, Biofabrication 5, 035001 (2013).
- 177. T. Billiet, E. Gevaert, T. De Schryver, M. Cornelissen, and P. Dubruel, Biomaterials **35**, 49 (2014).
- 178. Y. He, F. F. Yang, H. M. Zhao, Q. Gao, B. Xia, and J. Z. Fu, Scientific Reports **6**, 29977 (2016).
- 179. V. H. M. Mouser, F. P. W. Melchels, J. Visser, W. J. A. Dhert, D. Gawlitta, and J. Malda, Biofabrication **8**, 035003 (2016).
- 180. H. Yuk and X. Zhao, Advanced Materials 30, 1704028 (2018).
- 181. Y. Jin, D. Zhao, and Y. Huang, Bio-Design and Manufacturing 1, 123 (2018).
- 182. A. Blaeser, D. F. Duarte Campos, U. Puster, W. Richtering, M. M. Stevens, and H. Fischer, Advanced healthcare materials **5**, 326 (2016).
- 183. L. Ouyang, C. B. Highley, W. Sun, and J. A. Burdick, Advanced Materials **29**, 1604983 (2017).
- 184. Y. Zhao, Y. Li, S. Mao, W. Sun, and R. Yao, Biofabrication 7, 045002 (2015).

- 185. D. B. Kolesky, R. L. Truby, A. S. Gladman, T. A. Busbee, K. A. Homan, and J. A. Lewis, Advanced Materials **26**, 3124 (2014).
- 186. T. Bhattacharjee, S. M. Zehnder, K. G. Rowe, S. Jain, R. M. Nixon, W. G. Sawyer, and T. E. Angelini, Science advances 1, e1500655 (2015).
- 187. T. J. Hinton, Q. Jallerat, R. N. Palchesko, J. H. Park, M. S. Grodzicki, H. J. Shue, M. H. Ramadan, A. R. Hudson, and A. W. Feinberg, Science Advances 1, e1500758 (2015).
- 188. T. J. Hinton, A. Hudson, K. Pusch, A. Lee, and A. W. Feinberg, Acs Biomaterials Science & Engineering 2, 1781 (2016).
- 189. C. S. O'Bryan, T. Bhattacharjee, S. R. Niemi, S. Balachandar, N. Baldwin, S. T. Ellison, C. R. Taylor, W. G. Sawyer, and T. E. Angelini, Mrs Bulletin 42, 571 (2017).
- 190. J. T. Muth, D. M. Vogt, R. L. Truby, Y. Menguc, D. B. Kolesky, R. J. Wood, and J. A. Lewis, Advanced Materials **26**, 6307 (2014).
- 191. H. Gudapati, J. Yan, Y. Huang, and D. B. Chrisey, Biofabrication 6, 035022 (2014).
- 192. K. Pataky, T. Braschler, A. Negro, P. Renaud, M. P. Lutolf, and J. Brugger, Advanced Materials **24**, 391 (2012).
- 193. F. Xu, S. Moon, A. E. Emre, E. S. Turali, Y. S. Song, S. A. Hacking, J. Nagatomi, and U. Demirci, Biofabrication **2**, 014105 (2010).
- 194. T. Xu, K. W. Binder, M. Z. Albanna, D. Dice, W. Zhao, J. J. Yoo, and A. Atala, Biofabrication 5, 015001 (2013).
- 195. S. Moon, S. K. Hasan, Y. S. Song, F. Xu, H. O. Keles, F. Manzur, S. Mikkilineni, J. W. Hong, J. Nagatomi, and E. Haeggstrom, Tissue Engineering Part C-methods 16, 157 (2010).

- 196. A. Skardal, D. Mack, E. Kapetanovic, A. Atala, J. D. Jackson, J. Yoo, and S. Soker, Stem Cells Translational Medicine 1, 792 (2012).
- 197. U. A. Gurkan, R. E. Assal, S. Yildiz, Y. Sung, A. J. Trachtenberg, W. P. Kuo, and U. Demirci, Mol Pharm 11, 2151 (2014).
- 198. G. Gao, T. Yonezawa, K. Hubbell, G. Dai, and X. Cui, Biotechnology Journal 10, 1568 (2015).
- 199. X. Cui, K. Breitenkamp, M. Lotz, and D. D'Lima, Biotechnology & Bioengineering **109**, 2357 (2012).
- 200. B. Guillotin, A. Souquet, S. Catros, M. Duocastella, B. Pippenger, S. Bellance, R. Bareille,
 M. Rémy, L. Bordenave, and J. Amédée, Biomaterials 31, 7250 (2010).
- 201. L. Koch, S. Kuhn, H. Sorg, M. Gruene, S. Schlie, R. Gaebel, B. Polchow, K. Reimers, S. Stoelting, and N. Ma, Tissue Engineering Part C-Methods 16, 847 (2010).
- 202. L. Koch, A. Deiwick, S. Schlie, S. Michael, M. Gruene, V. Coger, D. Zychlinski, A. Schambach, K. Reimers, and P. M. Vogt, Biotechnology & Bioengineering 109, 1855 (2012).
- 203. N. R. Schiele, D. B. Chrisey, and D. T. Corr, Tissue Engineering Part C-Methods 17, 289 (2011).
- 204. N. E. Fedorovich, J. R. De Wijn, A. J. Verbout, J. Alblas, and W. J. Dhert, Tissue Engineering Part A 14, 127 (2008).
- 205. D. F. Duarte Campos, A. Blaeser, M. Weber, J. Jã¤Kel, S. Neuss, W. Jahnen-Dechent, and H. Fischer, Biofabrication **5**, 015003 (2013).
- 206. J. S. Lee, J. M. Hong, J. W. Jung, J. H. Shim, J. H. Oh, and D. W. Cho, Biofabrication 6, 024103 (2014).

- 207. Y. Zhang, Y. Yu, and I. T. Ozbolat, Journal of Nanotechnology in Engineering & Medicine 4, 021001 (2013).
- 208. M. T. Poldervaart, H. Wang, d. S. J. Van, H. Weinans, S. C. Leeuwenburgh, Ö. FC, W. J. Dhert, and J. Alblas, Plos One 8, e72610 (2013).
- 209. N. E. Fedorovich, W. Schuurman, H. M. Wijnberg, H. J. Prins, P. R. van Weeren, J. Malda, J. Alblas, and W. J. Dhert, Tissue Engineering Part C Methods 18, 33 (2012).
- 210. R. Gaetani, P. A. Doevendans, C. H. Metz, J. Alblas, E. Messina, A. Giacomello, and J. P. Sluijter, Biomaterials 33, 1782 (2012).
- 211. C. M. Smith, A. L. Stone, R. L. Parkhill, R. L. Stewart, M. W. Simpkins, A. M. Kachurin, W. L. Warren, and S. K. Williams, Tissue Engineering 10, 1566 (2004).
- 212. W. Xu, X. Wang, Y. Yan, W. Zheng, Z. Xiong, F. Lin, R. Wu, and R. Zhang, Journal of Bioactive & Compatible Polymers 22, 363 (2007).
- 213. X. Wang, Y. Y. Yan, Z. Xiong, H. Liu, J. Cheng, F. Liu, F. Lin, R. Wu, R. Zhang, and Q. Lu, Tissue Engineering Part A 12, 83 (2006).
- 214. A. Skardal, J. Zhang, L. Mccoard, X. Xu, S. Oottamasathien, and G. D. Prestwich, Tissue Eng Part A 16, 2675 (2010).
- 215. J. E. Snyder, Q. Hamid, C. Wang, R. Chang, K. Emami, H. Wu, and W. Sun, Biofabrication 3, 034112 (2011).
- 216. N. E. Fedorovich, H. M. Wijnberg, W. J. Dhert, and J. Alblas, Tissue Engineering Part A 17, 2113 (2011).
- 217. S. Hong, D. Sycks, H. F. Chan, S. Lin, G. P. Lopez, F. Guilak, K. W. Leong, and X. Zhao, Advanced Materials 27, 4034 (2015).